

Chapter 4

Nickel Fluoride Passivation of Nickel

4.1 Abstract

There is considerable interest in understanding and enhancing the passivation performance of nickel alloys in fluorine environments, unfortunately, experimental data is currently limited. Consequently, the point defect and transport properties of nickel fluoride (NiF_2) have been predicted using energy minimisation techniques. Results suggest that the dominant intrinsic defect reaction is anion Frenkel; however, formation energies are sufficiently high to suggest that defect concentrations are low. The lowest predicted saddle point energies are consistent with fluorine interstitial defects being transported along the c-axis. Formation of a split interstitial configuration is predicted. Simulation of impurities in NiF_2 lead to the suggestion that a novel nickel alloy, $\text{Ni}(\text{Li,Cu,Mg,Co,Mn})$, will form the least defective passivation layer with low concentrations of mobile fluorine interstitials. Alloy chemistry is arrived at via an analysis of calculated defect energies in NiF_2 , establishing solution limits for alloy additions and identifying those elements that modify the concentration of defects thought responsible for bulk transport. It is found to be particularly important to avoid the incorporation of 3+ cation forming elements such as iron.

4.2 Introduction

Industrial processes that use strong acids present significant challenges to material selection. Elevated processing temperature and pressure often negate the use of inert polymeric materials, while cost may inhibit the use of exotic coatings. Here the specific example is considered where hydrofluoric acid must be contained by a mechanically strong metal. Certain nickel alloys are known to offer corrosion resistance in fluoridating environments by the formation of a passive nickel fluoride layer. This study investigates the important mechanisms within this passive film and bases materials design recommendations on the results.

A NiF_2 passivation layer will form when nickel is subjected to a highly fluoridating environment [41–43]. In such circumstances the integrity of this layer depends critically on transport through the film since a passive layer does not provide a thermodynamic barrier to growth, but causes overwhelming kinetic hindrance. At elevated temperatures increased kinetics result in film growth and loss of protection. Any reduction in the transport kinetics within a film should benefit the system by increasing protection or extending the working temperature range at a given level of protection.

General texts [44, 45] indicate that there are substantial differences in passivation performance between different nickel alloy chemistries in fluoridating environments. The Monel 400 alloy is regarded as perhaps the best nickel alloy for hydrofluoric acid containment and is used industrially for the transport of liquid fluorine.

Atomistic simulation techniques are used to predict intrinsic defect energies and intrinsic defect migration saddle point energies. When information about impurity ion solution mechanisms is added, a detailed theory explaining the behaviour of NiF_2 as a passivation system can be formulated. Thus, stabilising or destabilising effects of alloying additions, from the underlying nickel metal can be predicted. In this way detrimental

elements (i.e. those which increase transport through the film) can be identified and excluded from the alloy. Likewise those elements that either reduce or have no effect on transport can also be identified. From the list of non-detrimental elements, appropriate alloy additions may be selected for improved mechanical strength without the risk of a deleterious effect on the passivation performance of the alloy. The resulting alloy may find an application in future fluorine compound containment systems where materials must not only be corrosion resistant but mechanically durable in case of accidents.

It is important to recognise the assumptions made in this analysis. A single crystal approach is taken, however, in reality the film may be polycrystalline. Thus, grain boundaries may be fast routes for migration circumventing the bulk lattice mechanisms considered here. Nevertheless, the single crystal approach still provides insight into important limiting bulk processes. In addition, the defect energies can be used to establish solution limits and thereby avoid impurity contents so great that second phase formation occurs. Any second phase will introduce complex grain boundary structures which will offer fast routes for transport. As such this approach details the optimum chemistry to limit complex grain boundary formation.

Relative saddle point energies for migration hops are generally a good indicator of the relative mobility of point defects in the lattice. It is accepted that other factors influence the mobility of defects in ionic materials, in particular those that contribute to the pre-exponential factors in the diffusion coefficient (see equation 1.6 and accompanying text in chapter 1). However, since only the relative mobility is required, saddle point energies should give an appropriate estimation without the necessity of using more complex (and computationally expensive) techniques such as molecular dynamics or even Monte Carlo simulations.

Finally, this atomistic simulation approach does not take into account electronic defects. However, due to the fact that NiF_2 is a highly ionic lattice it is unlikely that electronic

defects will be of any great significance. Similarly magnetic ordering in NiF₂ will not be an issue since operating temperatures will be above the Curie temperature (73K [46, 47]). Finally, a fully ionic model is assumed despite the suggestion by other workers that there is some covalency [46, 48]. Experience with fluorides suggests that even molecular species are highly ionic [49].

4.2.1 Crystallography

The lattice parameters for NiF₂ have been established during several investigations [50–52]. The lattice exhibits the rutile structure, space group D_{4h}^{14} (P4/mnm) in which atoms adopt the following Wychoff coordinates [53]:

$$\begin{aligned} \text{Ni: } & (0, 0, 0); \quad \left(\frac{1}{2}, \frac{1}{2}, \frac{1}{2}\right) \\ \text{F: } & \pm \left[(u, u, 0); \quad \left(u + \frac{1}{2}, \frac{1}{2} - u, \frac{1}{2}\right) \right] \\ & u = 0.302 \end{aligned}$$

This structure can be considered as a body centred tetragonal lattice of nickel ions which are octahedrally coordinated by fluorine ions (see figure 4.1). Nickel fluoride is known to undergo a phase transformation to an orthorhombic structure at elevated pressure [54], however, operating pressures for fluoride containment are not expected to approach that needed to trigger this transformation.

A feature of this lattice are the columns of octahedral interstitial sites along the c-axis (see figure 4.2). Initially these columns of interstitial sites appear as likely low energy migration pathways.

4.2.2 Physical Properties

Some physical properties have been established for the NiF₂ lattice. The vapour pressure has been investigated experimentally by Brunetti and Piacente [55] and Cantor [56]. Elastic constants are given in Landolt-Börnstein [57]. No other properties of the nickel fluoride

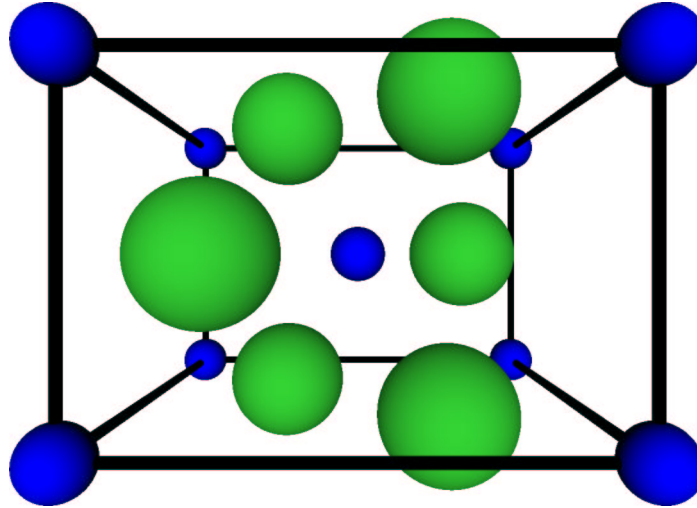


Figure 4.1: The tetragonal NiF_2 unit cell. Shown here, the a-axis is horizontal and the c-axis is vertical. Large green spheres are fluorine ions and small blue spheres are nickel ions.

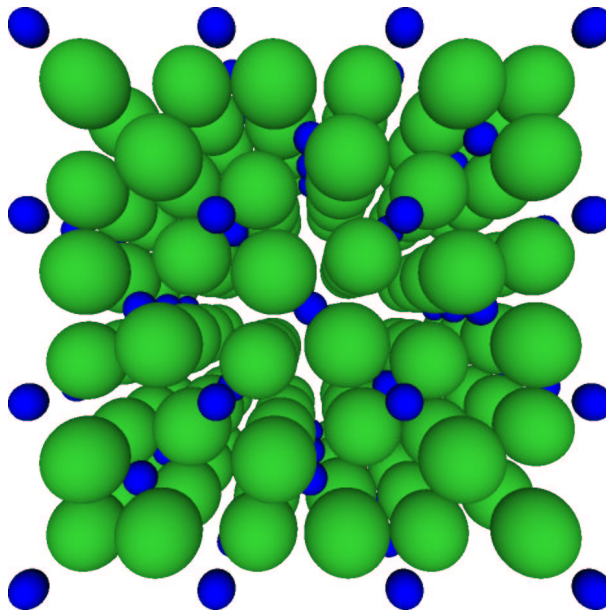


Figure 4.2: A view in the c-axis direction of a $3 \times 3 \times 3$ unit cell block of NiF_2 , the columns of octahedral interstitial sites along the c-axis can be seen.

lattice have been found.

4.2.3 Transport Properties

Jarry *et al.* [58], who studied NiF₂ film growth on nickel in a fluorine atmosphere, concluded that the rate of reaction follows a parabolic rate law. Thus, diffusion is of either a metal or non-metal through the adherent fluoride scale. They further show that fluorine is the active species, however, they were unable to determine the transport mechanism.

4.2.4 Simulation

Lattice simulations were carried out using the CASCADE [59] code which employs the methodology described in chapter 3. In order to simulate extrinsic defects, potentials that describe the short range interaction between F⁻ anions and the various dopant cations are required. While previous work [12, 60, 61] reports various potentials that could be used, many new potentials are required to maintain consistency with a common F⁻-F⁻ potential. Thus a completely new set of potentials was developed specifically for this study. Starting with the potential set of Cormack *et al.* [61] a modified F⁻-F⁻ potential was established. A new potential was developed since exact reproduction of the lattice c/a ratio was not achieved by the Cormack potential. The modified potential is still unable to exactly reproduce the tetragonal lattice, however it does represent a significant improvement over that of Cormack. With this new F⁻-F⁻ potential a full set of cation-F⁻ potentials were also developed to reproduce a wide range of fluoride materials. These potentials have already been presented in chapter 3, table 3.2. In the majority of cases these potentials have been fitted to several structures at the same time, thus reflecting the potential over a range of ion separations. This is important because, when defects are introduced, relaxed ion separations will be different than those seen in the equilibrium host lattice.

The results presented here are similar to those obtained by Cormack *et al.* for MgF_2 and MnF_2 . However, since Ni^{2+} is a d^8 open shell cation, ligand-field energies will need to be included if there is a change in the symmetry of the Ni^{2+} ion [62].

The extrinsic ions chosen were 1+, 2+ and 3+ cations with a range of ionic radii for each valence. This allows prediction of trends in behaviour as a function of dopant ion radii. Furthermore, once a trend is established, energies associated with ions not included in this study can be extrapolated.

4.3 Defect Chemistry

4.3.1 Defect Process model and Equations

Both intrinsic and extrinsic defect processes are important to this study. Consider the equations that describe the intrinsic defect equilibria in NiF_2 . These are the Schottky (reaction 4.1), anion Frenkel (reaction 4.2) and cation Frenkel (reaction 4.3) disorder processes.

Intrinsic Defect Reactions:



In order to compare results for these intrinsic reactions the calculated total energies must be normalised by a factor derived from a mass action analysis [63, 64]. Consider the intrinsic anion Frenkel disorder, reaction 4.2, as an example; the corresponding mass action equation for defect concentrations takes the form,

$$[\text{F}_{\text{i}}'][\text{V}_{\text{F}}^{\bullet}] = e^{\frac{-\Delta H_{\text{an-fren}}}{kT}} \quad (4.4)$$

where $\Delta H_{an-fren}$ is the predicted internal energy for reaction 4.2, k is the Boltzmann constant and T is the temperature. This involves both fluorine vacancy and interstitial concentrations. However, if the anion Frenkel reaction is dominant the electroneutrality condition can be invoked,

$$[F_i'] = [V_F^\bullet] \quad (4.5)$$

substitution of equation 4.5 into equation 4.4 yields an expression for the concentration of only one species,

$$[F_i'] = e^{\frac{-\Delta H_{an-fren}}{2kT}} \quad (4.6)$$

or,

$$[V_F^\bullet] = e^{\frac{-\Delta H_{an-fren}}{2kT}} \quad (4.7)$$

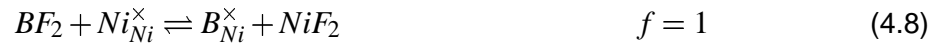
The normalisation factor for reaction 4.2 is thus two (from the denominator in the exponential), as is the normalisation for reaction 4.3. Through a similar analysis the energy for reaction 4.1 has a normalisation factor of three. The energy term, in concentration relationships, is the dominant variable. Thus, by comparing energies for different mechanisms, the lowest normalised energy reaction energy indicates the the dominant intrinsic mechanism, at equilibrium.

To consider the effect that alloy impurities and deliberate alloy additions have on the NiF₂ passivation layer, two aspects are important: the solution energy of the extrinsic elements and the charge compensating defects that are produced. Both of which are accessible from appropriate defect reactions.

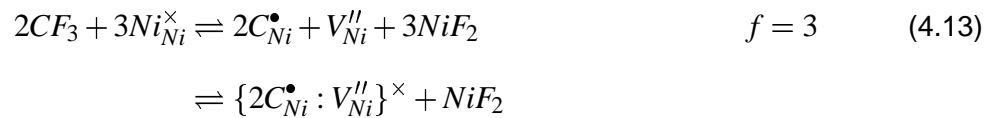
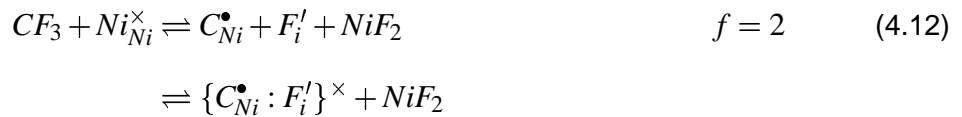
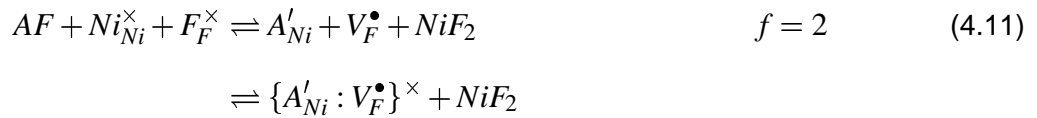
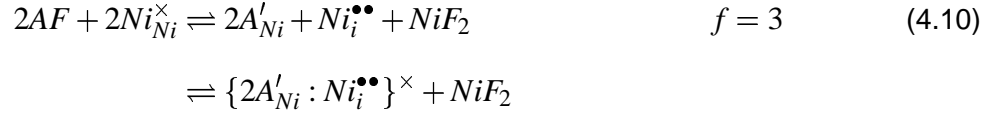
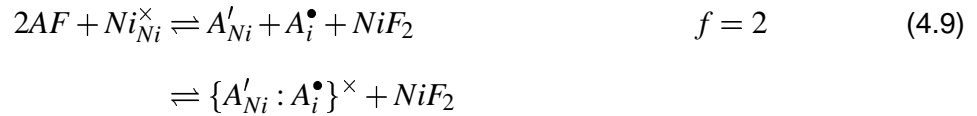
Equations 4.8-4.13 detail the important solution reactions for NiF₂ where A, B and C denote a dopant ion charge of 1+, 2+ or 3+ respectively. The isovalent solution reaction (equation 4.8) describes 2+ cation incorporation where no charge compensation is required. In the case of 1+ aliovalent cation solution, three reactions are considered corresponding to : dopant interstitial (equation 4.9), nickel interstitial (equation 4.10) and

fluorine vacancy (equation 4.11) compensation. For 3+ aliovalent cation solution two reactions are considered: fluorine interstitial (equation 4.12) and nickel vacancy (equation 4.13) compensation. The energies calculated for these reactions are subject to normalisation factors, f , which are calculated in a similar manner to the example given above for the intrinsic anion Frenkel reaction. These values are provided alongside the appropriate reaction.

Isovalent Solution Reactions:



Aliovalent Solution Reactions:



4.3.2 Solution Limits

Solution energies can be used to predict equilibrium solution concentrations for impurities in NiF_2 derived from the alloy additions. This provides a limit on the concentration of impurities to avoid second phase formation. Assuming a service temperature of 500°C the equilibrium concentration of an impurity $\frac{n}{N}$, can be approximated as,

$$\frac{n}{N} = e^{\frac{-\Delta H}{773k}} \quad (4.14)$$

where k is the Boltzmann's constant (8.62×10^{-5} eV/atom-K).

Since defect energies are normalised, the above equation can be used to estimate the concentration limit, thereby forging a link between defect energies and defect concentrations in the passivation layer. By further assuming that during film formation the levels of elements present in the passive layer reflects the alloy composition, a link is formed to the alloy chemistry.

In order to make this link, a judgement must be made about sensible addition levels for alloying elements. The following is reasonable based on typical nickel alloy chemistries [65]. Elements with solution limits below 0.05% [or 500ppm] (i.e. corresponding to solution energies above approximately 0.5eV in NiF_2) are likely to contribute to a second phase in NiF_2 and so cannot be tolerated in a substrate nickel alloy regardless of their effect on defect equilibria. Elements with solution limits above 0.05% and up to 2.5% [or 25,000ppm] (i.e. corresponding to solution energies of approximately 0.25eV in NiF_2) may be present in significant concentration without forming a second phase. Thus, if desirable, they may be tolerated as minor alloying additions to the substrate nickel alloy. Elements with solution limits above 2.5% (and obviously those that form solid solutions) can be incorporated into the NiF_2 lattice in very significant numbers. As such, these elements can be used as major alloying additions to the substrate nickel alloy provided they have a beneficial effect on the defect equilibria.

Combined with the knowledge of which defects will be produced by compensation reactions and the intrinsic defect equilibria, a prediction can be made about how additions will change the concentration of species which may limit or enhance transport. Additional knowledge of solution limits will allow sensible levels of alloy additions to be chosen.

4.3.3 Cluster Geometries

If dopant ions are aliovalent (i.e. exhibit a charge that is different to that of the lattice ion usually at that site) then oppositely charged compensating defects will be created to maintain charge neutrality in the lattice. Two cases can be considered: where the defects are spatially separated (i.e. are electrostatically isolated) or in close proximity (i.e. form a bound cluster). Cluster formation is primarily a consequence of coulombic attraction between charged defects. However, cooperative relaxation around defects in specific geometries can lead to a reduction in the overall strain introduced into the lattice, further favouring cluster formation and reducing the overall solution energy. Consequently, it is important to consider all possible cluster configurations in order to reliably predict the lowest energy and therefore most favourable solution mechanism. Here, clusters with defects arranged out to the third neighbour are simulated. Experience has shown that beyond the third neighbour the coulomb energy benefit from clustering is so reduced that specific defect orientations are never favoured over those with closer separations. This is fortunate since the number of possible configurations increases rapidly with the range of interactions considered!

Since in the NiF₂ lattice all cations are equivalent the substitutional ion is assigned to the position $(\frac{1}{2}, \frac{1}{2}, \frac{1}{2})$ without loss of generality. In the following description all positions are given in terms of fractional unit cell parameters.

4.3.3.1 Monovalent Dopant Interstitial Clusters

In this solution mechanism a monovalent dopant interstitial will compensate the solution of a monovalent cation substitutional, $\{A'_{Ni}:A_i^\bullet\}$. The substitutional ion, A'_{Ni} , is at $(\frac{1}{2}, \frac{1}{2}, \frac{1}{2})$ and the compensating dopant interstitials are then arranged in the positions give in table 4.1.

4.3.3.2 Monovalent Interstitial Clusters

In this solution mechanism a nickel interstitial ion will compensate the solution of two monovalent cation substitutional ions to form $\{2A'_{Ni}:Ni_i^{\bullet\bullet}\}$. The compensating interstitial ion, $Ni_i^{\bullet\bullet}$, will occupy the $(\frac{1}{2}, 0, 0)$ site and the substitutional monovalent cations are arranged in the positions given in table 4.2.

4.3.3.3 Monovalent Vacancy Clusters

In this solution mechanism a fluorine vacancy will compensate the solution of a monovalent cation substitutional ion to form $\{A'_{Ni}:V_F^\bullet\}$. The substitutional ion, A'_{Ni} , will occupy the $(\frac{1}{2}, \frac{1}{2}, \frac{1}{2})$ site and the compensating fluorine vacancy defects are arranged in the positions given in table 4.3.

4.3.3.4 Trivalent Interstitial Clusters

In this solution mechanism a fluorine interstitial will compensate the solution of a trivalent cation substitutional ion to form $\{C_{Ni}^\bullet:F'_F\}$. The substitutional ion, C_{Ni}^\bullet , will occupy $(\frac{1}{2}, \frac{1}{2}, \frac{1}{2})$ and the compensating fluorine interstitial ions are arranged in the positions given by table 4.4 ¹.

¹Since the fluorine interstitial adopts a split configuration the defect site is considered to be located on a fluorine lattice site, which is mid way between the split interstitials.

4.3.3.5 Trivalent Vacancy Clusters

In this solution mechanism a nickel vacancy will compensate the solution of two trivalent cation substitutionals to form $\{2C_{Ni}^{\bullet}:V_{Ni}''\}$. The compensating nickel vacancy, V_{Ni}'' , is at $(\frac{1}{2}, \frac{1}{2}, \frac{1}{2})$ and the cation substitutional ions are arranged in the positions given by table 4.5.

Table 4.1: Monovalent dopant interstitial cluster configurations: position of dopant interstitial defects relative to a cation substitutional site at $(\frac{1}{2}, \frac{1}{2}, \frac{1}{2})$.

cluster	Position		
	x	y	z
1	$\frac{1}{2}$	0	$\frac{1}{2}$
2	$\frac{1}{2}$	0	0
3	$\frac{1}{2}$	0	$-\frac{1}{2}$

Table 4.2: Monovalent interstitial cluster configurations: position of cation substitutional defects relative to a nickel interstitial site at $(\frac{1}{2}, 0, 0)$.

cluster	1 st position			2 nd position		
	x	y	z	x	y	z
1-1	0	0	0	1	0	0
1-2a	0	0	0	$\frac{1}{2}$	$\frac{1}{2}$	$\frac{1}{2}$
1-2b	0	0	0	$\frac{1}{2}$	$-\frac{1}{2}$	$\frac{1}{2}$
1-3a	0	0	0	0	0	1
1-3b	0	0	0	1	0	1
2-2a	$\frac{1}{2}$	$\frac{1}{2}$	$\frac{1}{2}$	$\frac{1}{2}$	$\frac{1}{2}$	$-\frac{1}{2}$
2-2b	$\frac{1}{2}$	$\frac{1}{2}$	$\frac{1}{2}$	$\frac{1}{2}$	$-\frac{1}{2}$	$\frac{1}{2}$
2-2c	$\frac{1}{2}$	$\frac{1}{2}$	$\frac{1}{2}$	$\frac{1}{2}$	$-\frac{1}{2}$	$-\frac{1}{2}$
2-3a	$\frac{1}{2}$	$\frac{1}{2}$	$\frac{1}{2}$	0	0	1
2-3b	$\frac{1}{2}$	$\frac{1}{2}$	$\frac{1}{2}$	1	0	1
2-3c	$\frac{1}{2}$	$\frac{1}{2}$	$\frac{1}{2}$	0	0	-1
2-3d	$\frac{1}{2}$	$\frac{1}{2}$	$\frac{1}{2}$	1	0	-1
3-3a	0	0	1	1	0	1
3-3b	0	0	1	0	0	1
3-3c	0	0	1	1	0	-1

Table 4.3: Monovalent vacancy cluster configurations: position of fluorine vacancy defects relative to a cation substitutional site at $(\frac{1}{2}, \frac{1}{2}, \frac{1}{2})$.

cluster	Position		
	x	y	z
1	$\frac{1}{2}-u$	$\frac{1}{2}+u$	$\frac{1}{2}$
2	u	u	0
3	-u	0 -u	$\frac{1}{2}$

Table 4.4: Trivalent interstitial cluster configurations: position of split fluorine interstitial defects (centred on a fluorine lattice site) relative to a cation substitutional site at $(\frac{1}{2}, \frac{1}{2}, \frac{1}{2})$.

cluster	Position		
	x	y	z
1	$\frac{1}{2}-u$	$\frac{1}{2}+u$	$\frac{1}{2}$
2	u	u	0
3	$\frac{1}{2}-u$	$\frac{1}{2}+u$	$-\frac{1}{2}$
4	$\frac{1}{2}-u$	$u-\frac{1}{2}$	$\frac{1}{2}$
5	$1+u$	u	0

Table 4.5: Trivalent vacancy cluster configurations: position of cation substitutionals relative to a nickel vacancy site at $(\frac{1}{2}, \frac{1}{2}, \frac{1}{2})$.

cluster	1 st position			2 nd position		
	x	y	z	x	y	z
1-1	$\frac{1}{2}$	$\frac{1}{2}$	$-\frac{1}{2}$	$\frac{1}{2}$	$\frac{1}{2}$	$-\frac{3}{2}$
1-2b	$\frac{1}{2}$	$\frac{1}{2}$	$-\frac{1}{2}$	1	0	0
1-2c	$\frac{1}{2}$	$\frac{1}{2}$	$-\frac{1}{2}$	0	0	1
1-2d	$\frac{1}{2}$	$\frac{1}{2}$	$-\frac{1}{2}$	1	0	1
1-3a	$\frac{1}{2}$	$\frac{1}{2}$	$-\frac{1}{2}$	$-\frac{1}{2}$	$-\frac{1}{2}$	$-\frac{1}{2}$
2-2a	0	0	0	1	1	0
2-2b	0	0	0	1	0	0
2-2c	0	0	0	1	1	1
2-2d	0	0	0	1	0	1
2-2e	0	0	0	0	0	1
2-3a	0	0	0	$-\frac{1}{2}$	$\frac{1}{2}$	$\frac{1}{2}$
2-3b	0	0	0	$\frac{3}{2}$	$\frac{1}{2}$	$\frac{1}{2}$
3-3a	$-\frac{1}{2}$	$\frac{1}{2}$	$\frac{1}{2}$	$\frac{1}{2}$	$\frac{3}{2}$	$\frac{1}{2}$
3-3b	$-\frac{1}{2}$	$\frac{1}{2}$	$\frac{1}{2}$	$\frac{3}{2}$	$\frac{1}{2}$	$\frac{1}{2}$

4.4 Results and Discussion

4.4.1 Perfect Lattice Results

Table 4.6 reports predicted and experimental lattice parameters for the NiF₂ lattice. This shows good agreement with the experimental data, particularly the critical parameter of unit cell volume. A small error in the c/a ratio is often seen when simulating rutile structured materials. A brief investigation of this phenomenon was undertaken and is presented in appendix A. Here, the c/a error is small and as such will have only a very minor impact on the relative defect energies.

Table 4.6: Calculated and experimental lattice parameters for NiF₂.

	a (Å)	c (Å)	$\frac{c}{a}$	Volume (Å ³)
<i>Calc.</i>	4.585	3.172	0.692	66.683
<i>Expt.</i> [50–52]	4.6506	3.0836	0.663	66.692
<i>error</i>	–1.41%	2.87%	4.37%	–0.01%

Predicted bulk elastic constants are given in table 4.7 and again show good agreement with experiment particularly for the diagonal terms of the elastic tensor. Finally the predicted dielectric constants are presented in table 4.8. Unfortunately no experimental data is available for comparison.

Table 4.7: Calculated and experimental elastic constants ($\times 10^{11}$ dyne cm^{–2}) for NiF₂.

	C ₁₁	C ₁₂	C ₁₃	C ₃₃	C ₄₄	C ₆₆
<i>Calc.</i>	13.24	9.15	6.66	21.45	5.72	9.31
<i>Expt.</i> [57]	14.5	11.0	9.1	22.1	4.65	9.94

Table 4.8: Calculated dielectric properties for NiF₂.

ϵ_s^{11}	ϵ_s^{33}	ϵ_∞^{11}	ϵ_∞^{33}
5.94	5.01	1.85	1.85

The quality of the predicted perfect lattice results and elastic constants are excellent and provide confidence that the following defect energies will be representative of the system. However, some caution should be expressed about using predicted absolute values. Trends and relative results are therefore emphasised when drawing conclusions from these types of simulation rather than absolute values.

4.4.2 Intrinsic Defect Equilibria

Isolated defect energies were calculated for intrinsic vacancy and interstitial defects (see table 4.9). These energies were used to calculate the normalised formation energies for intrinsic defects via the various defect equilibria reported in equations 4.1-4.3 (see table 4.10). Values are consistent with anion Frenkel disorder being the dominant process. Thus, fluorine vacancies and interstitials will be the majority intrinsic defects. However, the Schottky disorder energy is only marginally higher. Schottky disorder may therefore provide important concentrations of defects which could contribute to transport if their associated activation energies are low.

Table 4.9: Intrinsic isolated defect formation energies (eV) for NiF₂.

V_F^\bullet	V_{Ni}''	F_i'	$Ni_i^{\bullet\bullet}$
5.874	25.965	-1.361	-17.367

Table 4.10: Normalised intrinsic equilibrium energies (eV) for NiF₂.

Schottky	Anion Frenkel	Cation Frenkel
2.59	2.26	4.30

While simulating fluorine interstitial defects, it was observed that they adopt a novel split-interstitial configuration similar to that found in MgF₂ and MnF₂ by Cormack *et al.* [61]. In this configuration the fluorine interstitial ion displaces a lattice fluorine ion into an adjacent interstitial site. Thus, two interstitial ions share the lattice vacancy that is created, as illustrated in figure 4.3. These defects remain confined to the ab plane.

4.4.3 Intrinsic Migration

Intrinsic migration of both cations and anions was considered via vacancy and interstitial mechanisms. This was achieved using the methodology for predicting saddle point energies, described in chapter 3. Fortunately, in the NiF₂ unit cell, all vacancy and interstitial sites are equivalent and as such a single site can be chosen as the start point for hop mechanisms of the same species. All possible hops will be defined by routes to neighbouring equivalent sites. Each migration hop is detailed below and summarised in table 4.11.

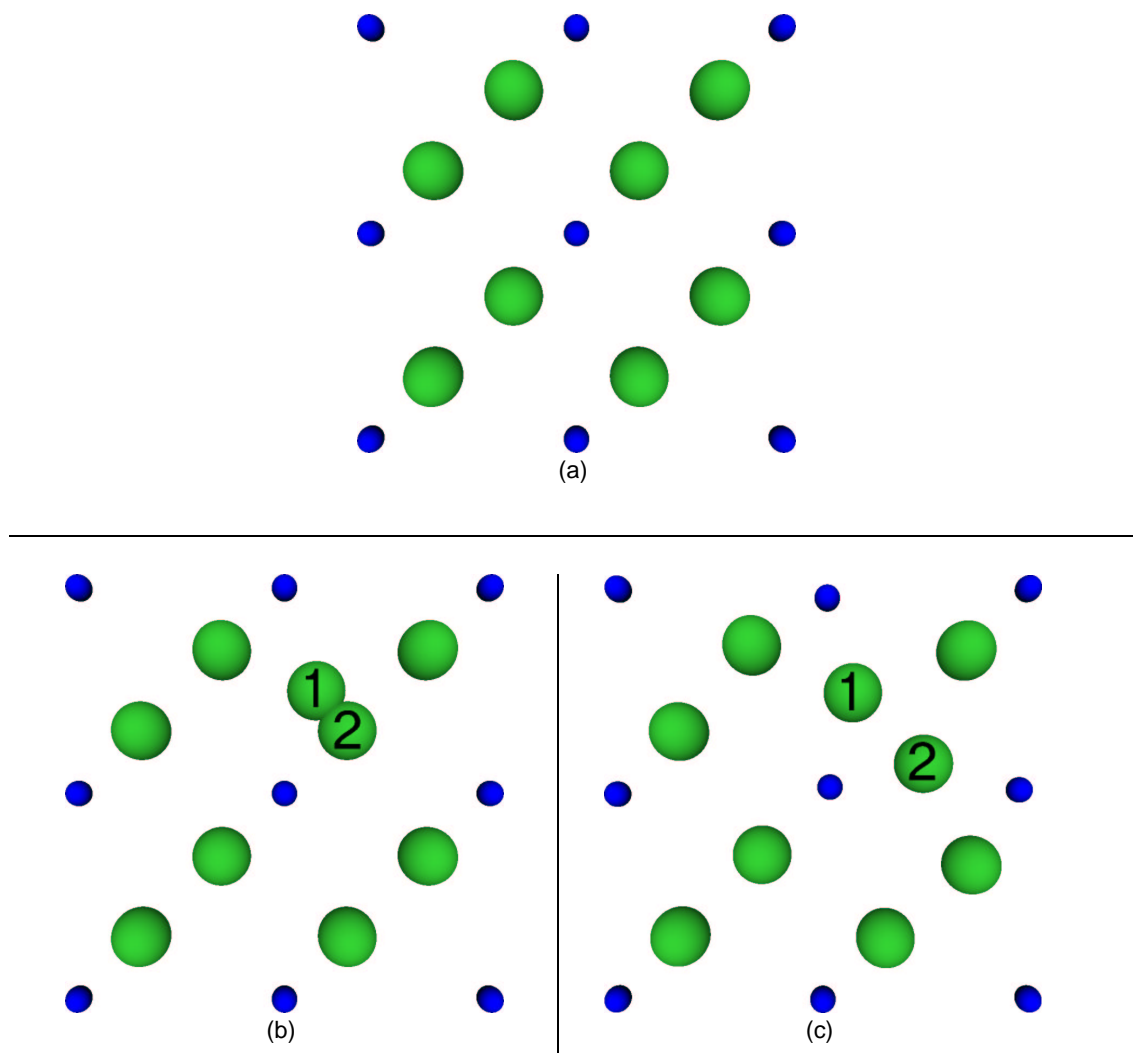


Figure 4.3: Illustration of the split fluorine interstitial configuration in NiF_2 . Representation is a 2×2 unit cell basal plane a) the perfect lattice, b) a fluorine interstitial (1) is introduced adjacent to a fluorine lattice site (2), pre-relaxation, c) post relaxation, the two ions (1 and 2) share a lattice vacancy previously occupied by fluorine ion (2).

Table 4.11: Migration energies in NiF₂. †This transport process is not continuous through the lattice (see section 3.3.3 for explanation).

Defect Species	Hop Direction	Activation Energy (eV)
V_F^\bullet	[001]	1.17
	[110]	0.25 [†]
	$[\overline{66} \ 1\overline{5} \ 1 \ 0]$	1.53
	$[125 \ \overline{2} \overline{4} \ 125]$	0.67
V_{Ni}''	[001]	0.87
	[111]	1.37
	[100]	1.41
F_i'	$[1 \ \overline{1} \ 5 \ 0]$	0.11
	$[\overline{7} \ \overline{8} \ 25]$	0.024
$Ni_i^{\bullet\bullet}$	[110]	0.74
	[001]	0.42

4.4.3.1 Fluorine Migration via a Vacancy Mechanism

Four possible fluorine migration pathways via a vacancy were identified and studied. All fluorine vacancy migration processes are taken to start with the vacancy at $(u, u, 0)$, in Wychoff coordinates. The activation energy is the difference between the defect energy where only one fluorine site is vacant (and the lattice ions are all allowed to relax to zero force) and the saddle point configuration. The defect energy calculated for an isolated fluorine vacancy is 5.874eV (see table 4.9).

Fluorine Vacancy Mechanism Number 1. This migration hop is to $(u, u, 1)$ which is in the [001] direction. The saddle point was found to be at $(0.26, 0.26, \frac{1}{2})$ and the defect energy at this point was calculated as 7.044eV. The activation energy for this migration is therefore 1.170eV (7.044eV - 5.874eV). It is possible for a defect to travel through the lattice via this mechanism alone, thus, it is a mode 1 migration hop as defined in section

3.3.3.

The contour plots in figure 4.4 show that the lowest energy pathway is not a straight line between the start and end point of the hop. This hop is not direct and the fluorine ion is displaced in the $[\bar{1}\bar{1}0]$ direction as it approaches the saddle point.

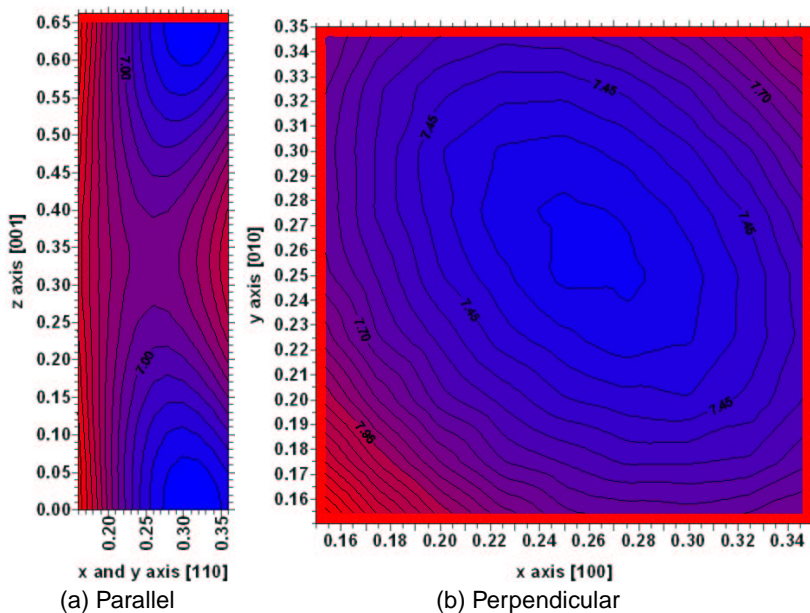


Figure 4.4: Energy contour plots parallel (a) and perpendicular (b) to a hop via fluorine vacancy mechanism 1.

The defect energy change as the migration hop proceeds is plotted in figure 4.5. This shows the energy to vary smoothly, increasing to a maximum which clearly identifies the saddle point energy.

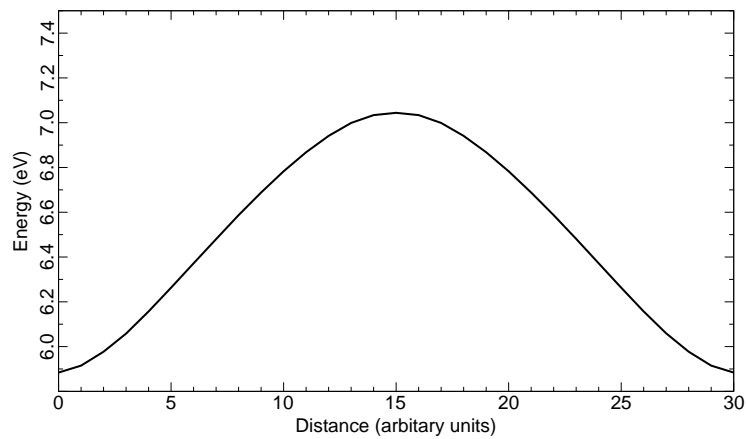


Figure 4.5: Activation energy plot for a hop via fluorine vacancy mechanism 1.

Fluorine Vacancy Mechanism Number 2. This migration pathway ends at $(\bar{u}, \bar{u}, 0)$ and is therefore in the $[110]$ direction. The saddle point was found to be at $(\frac{1}{2}, \frac{1}{2}, 0)$ and the defect energy at this point was calculated to be 6.126eV. The activation enthalpy for this migration hop is therefore 0.252eV (6.126eV - 5.874eV). After a hop of this type the only equivalent hop will return the defect back to the original site. As such, this is a mode 2 hop and transport of the defect over long distances can only proceed if this hop is part of a mode 3 hop (see section 3.3.3 for an explanation).

The contour plot in figure 4.6a shows the migration path between the start and end point. From this it is apparent that the migration is direct and the saddle point is at the mid-point on a direct line between the start and end point. This is confirmed in figure 4.6b.

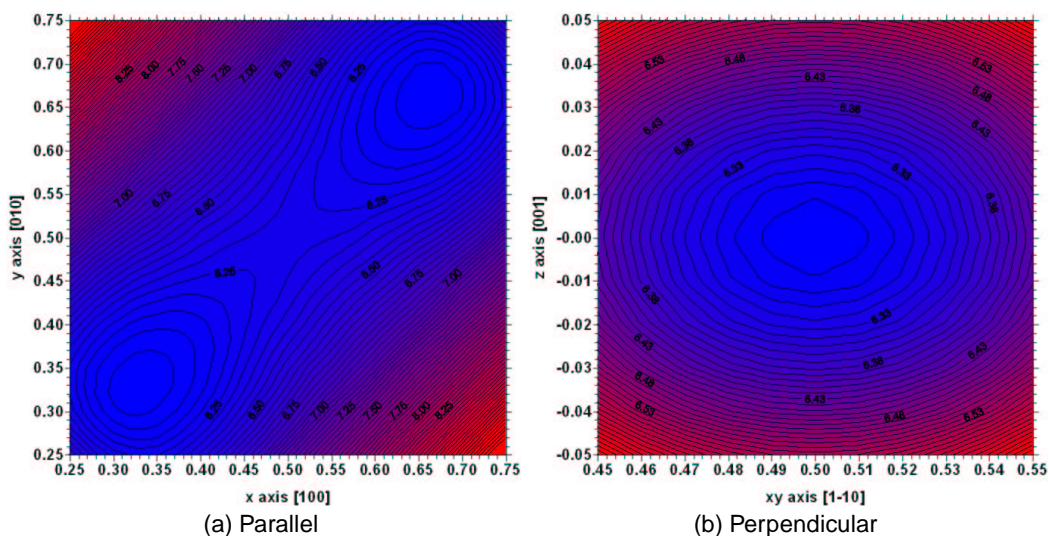


Figure 4.6: Energy contour plots parallel (a) and perpendicular (b) to a hop via fluorine vacancy mechanism 2.

The defect energy varies smoothly along the hop path and increases to an obvious maximum (see figure 4.7). The saddle point energy is thus easily identified for this pathway.

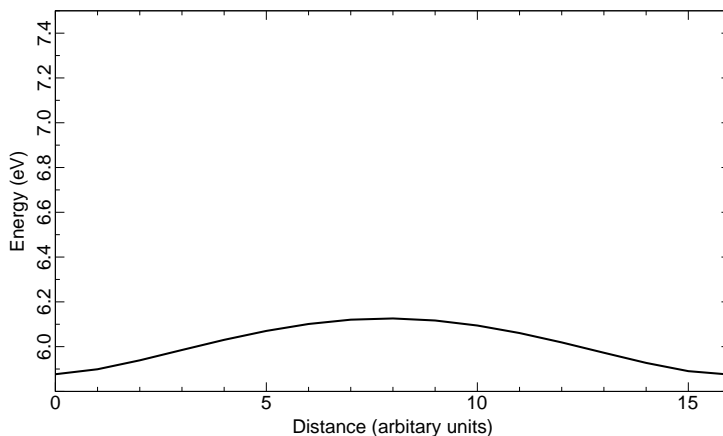


Figure 4.7: Activation energy plot for a hop via fluorine vacancy mechanism 2.

Fluorine Vacancy Mechanism Number 3. This migration is to $(1 - u, -u, 0)$ which is in the $[66\bar{1}510]$ direction. The saddle point was found to be at $(\frac{1}{2}, 0, 0)$ and the defect energy at this point was calculated to be 7.400eV. The activation enthalpy for this migration

is therefore 1.526eV (7.400eV - 5.874eV). This is a mode 1 hop.

The contour plot in figure 4.8 shows that the hop is not quite direct, deviating slightly from a straight line. This is indicated by minor asymmetry in the contour plot iso-energy lines, however, the migration pathway is still easily identified.

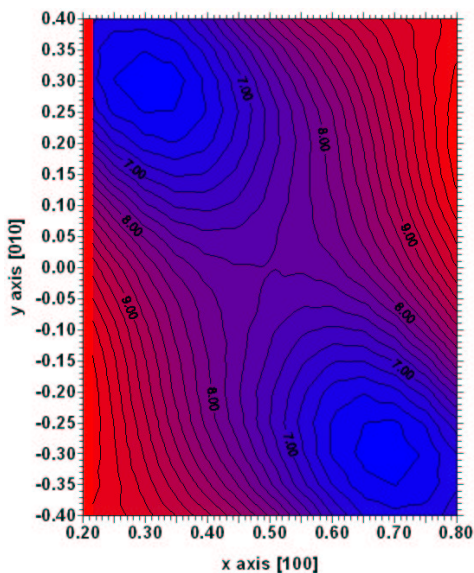


Figure 4.8: Energy contour plot parallel to a hop via fluorine vacancy mechanism 3.

The defect energy along the migration pathway varies smoothly to a maximum as shown in figure 4.9. Thus, despite the slightly indirect route the saddle point energy is easily established.

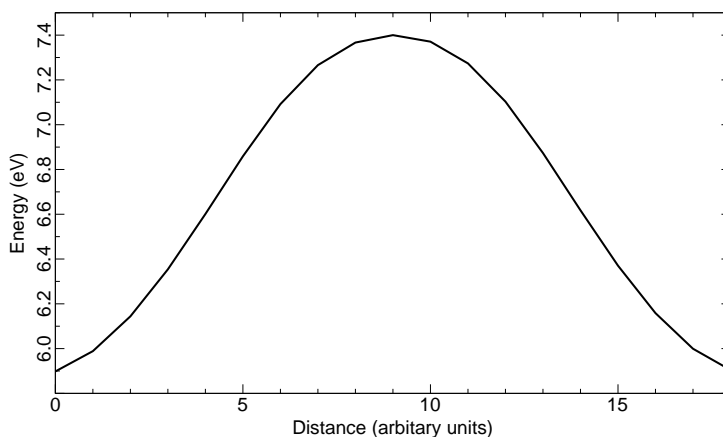


Figure 4.9: Activation energy plot for a hop via fluorine vacancy mechanism 3.

Fluorine Vacancy Mechanism Number 4. This migration is to $(\frac{1}{2} + u, \frac{1}{2} - u, \frac{1}{2})$ which is in the $[125 \bar{2}4 125]$ direction. The saddle point was found to be at (0.55, 0.23, 0.16) and the defect energy at this point was calculated to be 6.539eV. The activation enthalpy for this migration process is therefore 0.665eV (6.539eV - 5.874eV). Defect transport through the lattice is possible via this mechanism alone so it is a mode 1 hop. The non-orthogonal direction of this migration makes it difficult to show a contour plot for the whole migration, hence figure 4.10 shows a contour plot perpendicular to the migration path containing the saddle point. It should be noted that the migration path is not direct and deviates from a straight line between the start and end points of the process. Due to the non-regular geometry of this migration pathway, a full plot of the defect energy along the hop path was difficult to calculate and figure 4.11 only contains partial data for the critical region near the saddle point.

sites and a single nickel interstitial ion. The defect enthalpy calculated for an isolated nickel vacancy is 25.965eV (see table 4.9).

Nickel Vacancy Mechanism Number 1. This migration hop is to $(0, 0, 1)$ which is in the $[001]$ direction. The saddle point was found to be at $(0.068, 0.068, \frac{1}{2})$ and the defect energy at this point was determined to be 26.837eV. The activation enthalpy for this migration hop is therefore 0.872eV ($26.837\text{eV} - 25.965\text{eV}$). This is a mode 1 hop so no other mechanisms are required for defect transport through the lattice.

The contour plots in figure 4.12 detail the hop path between its migration start and end point. It is apparent that the hop is not direct but moves slightly in the $[110]$ direction as it approaches the saddle point.

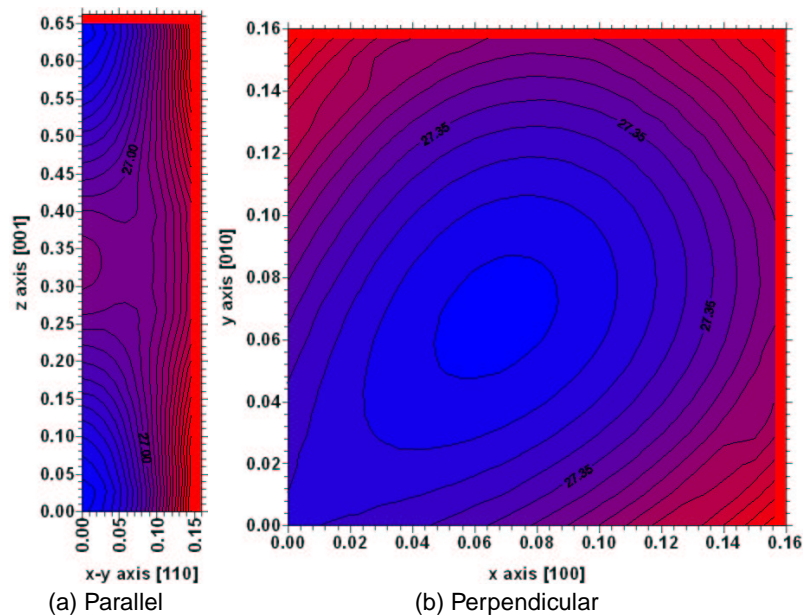


Figure 4.12: Energy contour plots parallel (a) and perpendicular (b) to a hop via nickel vacancy mechanism 1.

The defect energies along the hop path vary smoothly but plateau near the saddle point (see figure 4.13). While this could have indicated that there was a hidden metastable

position near the saddle point, a detailed investigation of the surrounding area revealed no such metastable point with the current resolution with this technique.

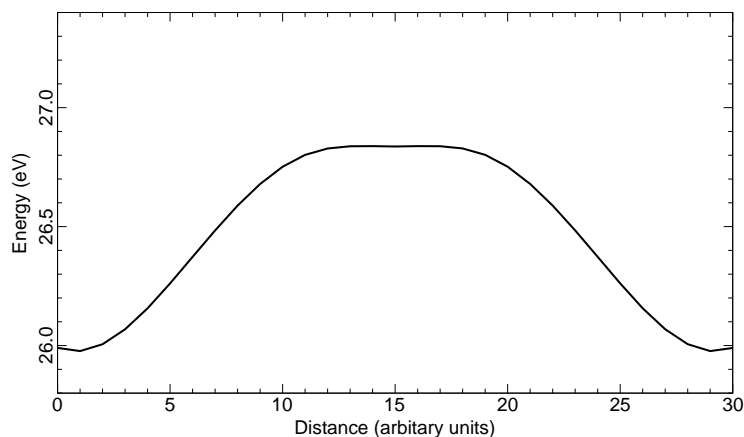


Figure 4.13: Activation energy plot for a hop via nickel vacancy mechanism 1.

Nickel Vacancy Mechanism Number 2. This migration is to $(\frac{1}{2}, \frac{1}{2}, \frac{1}{2})$ which is in the [111] direction. The saddle point was found to be at $(0.14, 0.14, 0.24)$ and the defect energy at this point determined is 27.332eV. The activation enthalpy for this migration process is therefore 1.367eV $(27.332\text{eV} - 25.965\text{eV})$. This is a mode 1 hop.

The contour plot in figure 4.14 indicates that the migration pathway deviates considerably from a straight line and takes a distinctly curved route. This makes sense when the crystallography is considered since the direct path is hindered by fluorine atoms.

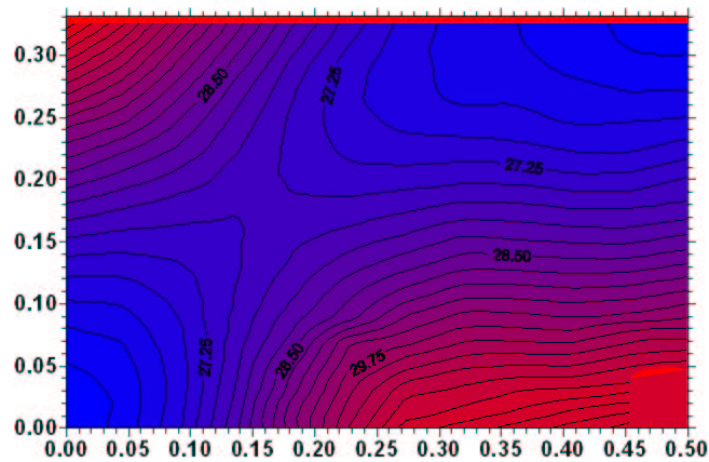


Figure 4.14: Energy contour plot parallel to a hop via nickel vacancy mechanism 2.

Figure 4.15 shows how the defect energy varies along the migration path. Note how the activation barrier is asymmetric. This is due to the indirect migration pathway shifting the saddle point closer to $(0,0,0)$. Despite this asymmetry the saddle point energy is easily identified.

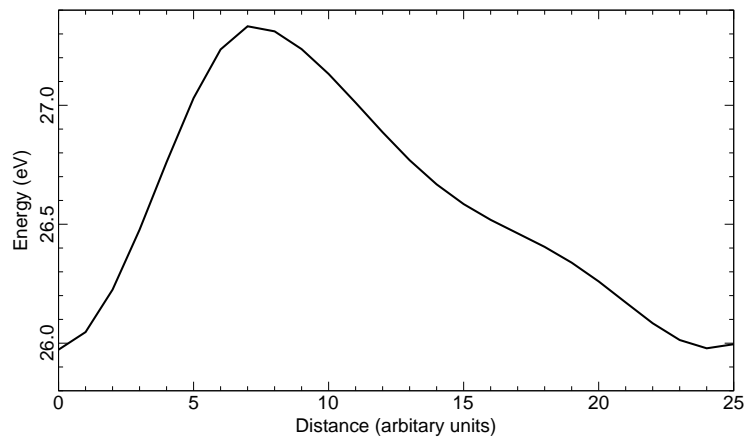


Figure 4.15: Activation energy plot for a hop via nickel vacancy mechanism 2.

Nickel Vacancy Mechanism Number 3. This migration is to $(1,0,0)$ which is in the $[100]$ direction. Two saddle points were found at $(0.35, 0.0, 0.0)$ and $(0.65, 0.0, 0.0)$. The

defect energy at these points is determined to be 27.372eV. The activation enthalpy for this migration is therefore 1.407eV (27.372eV - 25.965eV). Since transport can proceed through the lattice by this mechanism alone it is a mode 1 hop.

This migration exhibits two very interesting features, with reference to figures 4.16 and 4.17, the migration is not direct. The nickel ion remains in the basal plane but takes a slightly s-shaped path (compare a-c in figure 4.17 which are contour plots in the y-z plane at intervals along the x direction of the unit cell). The reason for this torturous route is made apparent if one considers the local arrangement of atoms in the crystal.

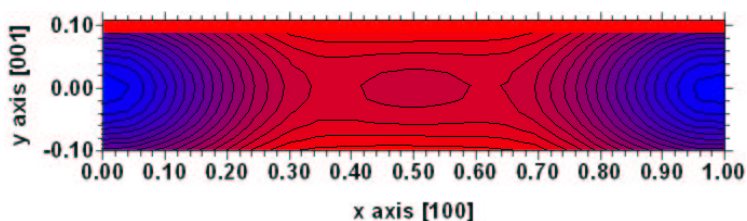


Figure 4.16: Energy contour plots parallel to a hop via nickel vacancy mechanism 3.

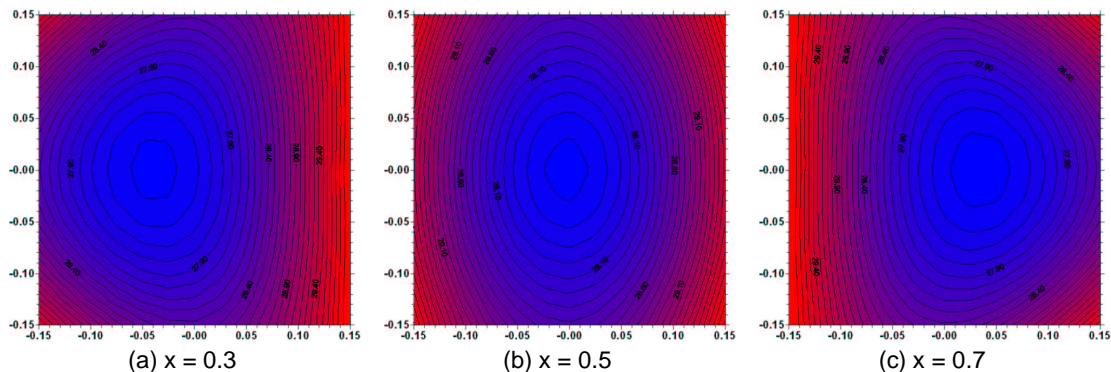


Figure 4.17: Energy contour plots perpendicular to a hop via nickel vacancy mechanism 3.

The variation in defect energy along the migration path, shown in figure 4.18, indicates the other interesting feature of this mechanism. This process appears to exhibit a metastable position at the mid point. This is perhaps not surprising as the path is directly

through an interstitial site. In this case there are two equivalent saddle points.

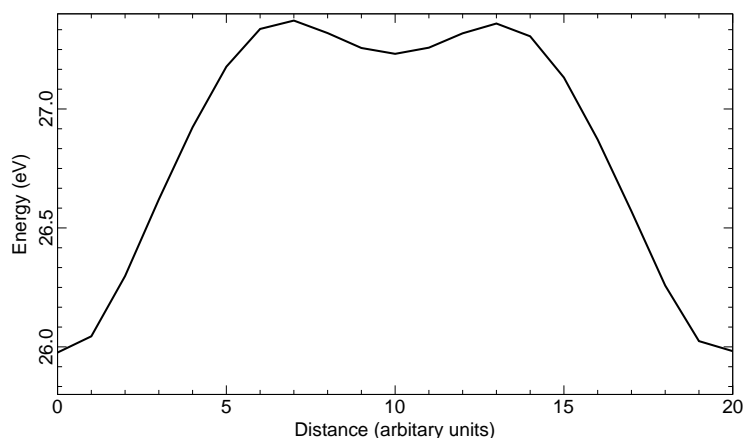


Figure 4.18: Activation energy plot for migration via nickel vacancy mechanism 3.

4.4.3.3 Fluorine Migration via an Interstitial Mechanism

Two possible fluorine interstitial migration mechanisms have been identified and investigated. Hops are taken to start at a single interstitial site which in this case is taken to be (0.49, 0.15, 0.00) in Wychoff coordinates. Migration proceeds via ion hops to adjacent interstitial sites. The activation energy is the difference between the defect energy assuming an isolated split fluorine interstitial defect with all the surrounding ions at their equilibrium positions and the saddle point configuration, which involves a single fluorine interstitial ion. The defect enthalpy calculated for an isolated fluorine interstitial is -1.361 eV (see table 4.9).

These migration calculations were significantly more difficult to perform than the other mechanisms. This is due to split interstitial formation, since the relaxation of the displaced fluorine in the split interstitial defect happens some distance from the path of the migration. Thus, it was necessary to do full region I size calculations for contour plots. Also, activation energies for these mechanisms are very low. Initially it might be thought that there are two possible migrations in the [001] direction, however, they are the

same by symmetry. Migration hop 1 is unusual and only occurs due to the formation of the split fluorine interstitial defect. Migration 2 is a more usual migration and calculations suggest it has a slightly lower activation energy than migration 1. However, the calculated activation energies for the two migrations are extremely low, indicating, migration is likely to be isotropic.

Fluorine Interstitial Mechanism 1. This migration hop is to $(0.51, -0.15, 0.0)$ which is in the $[1\bar{1}\bar{5}0]$ direction. The saddle point was found to be at $(\frac{1}{2}, \frac{1}{2}, 0)$ and the defect energy at this point was determined to be -1.249eV . The activation enthalpy for this migration hop is therefore 0.112eV ($-1.249\text{eV} - (-1.361\text{eV})$). Even with this unusual mechanism (due to the split interstitial) this is still a mode 1 hop.

The hop distance for this mechanism is surprisingly short and the mechanism somewhat complicated. The contour plot in figure 4.20 shows that this is a reasonably direct hop, the complexity comes from the surrounding lattice relaxation. This is best described by reference to the schematic diagrams of figure 4.19, which details the following steps:

- 1 : the migration begins with ions 1 and 2 forming a split interstitial defect in the top right unit cell (figure 4.19a).
- 2 : ion 2 migrates toward ion 3 into the bottom right unit cell.
- 3 : ion 1 relaxes onto the previously shared vacant lattice site while ion 3 moves into an interstitial site leaving behind a vacant site. Thus, ions 2 and 3 form a new split interstitial defect in the bottom right unit cell (figure 4.19b).

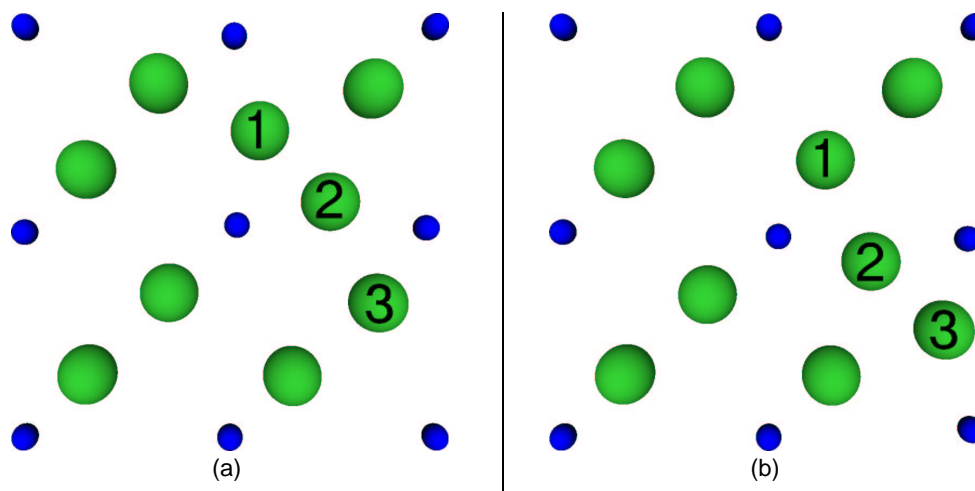


Figure 4.19: Illustration of split-interstitial migration in the ab plane represented in a 2×2 unit cell basal plane: a) the split interstitial is formed by two ions (1 and 2), b) ion 2 has moved towards ion 3 such that two interstitials (2 and 3) share a lattice vacancy previously occupied by 3 and ion 1 relaxes onto a lattice site.

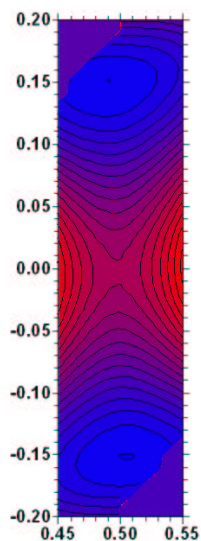


Figure 4.20: Energy contour plot parallel to a hop via fluorine interstitial mechanism 1.

The variation of defect energy along the hop is shown in figure 4.21. This indicates a smooth variation in energy to a distinct, and easily established maximum.

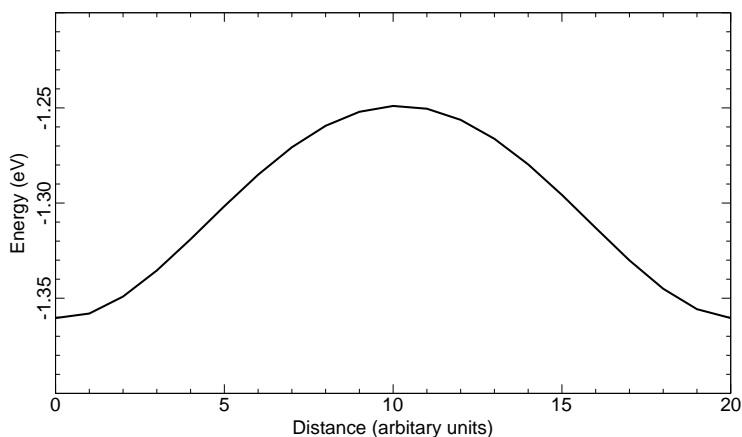


Figure 4.21: Activation energy plot for a hop via fluorine interstitial mechanism 1.

Fluorine Interstitial Mechanism 2. This migration is to $(0.35, -0.01, \frac{1}{2})$ which is in the $[\bar{7}\bar{8}25]$ direction. The saddle point was found to be at $(0.445, 0.045, 0.250)$ and the defect energy at this point was determined to be -1.337eV . The activation enthalpy for this migration hop is therefore 0.024eV ($-1.337\text{eV} - (-1.361)$). Transport of defects through the lattice is possible with this hop alone, thus it is a mode 1 hop.

The path of this migration is complex proceeding along the c-axis in a series of hops that spiral up the c-axis. Representative contour and energy barrier plots were impossible to construct and are not present. The migration pathway was established by calculating defect energies across multiple parallel ab planes. The minimum defect energy at each of these planes was assumed to be a point on the contiguous migration pathway and the maximum value of the data set was taken as the saddle point energy.

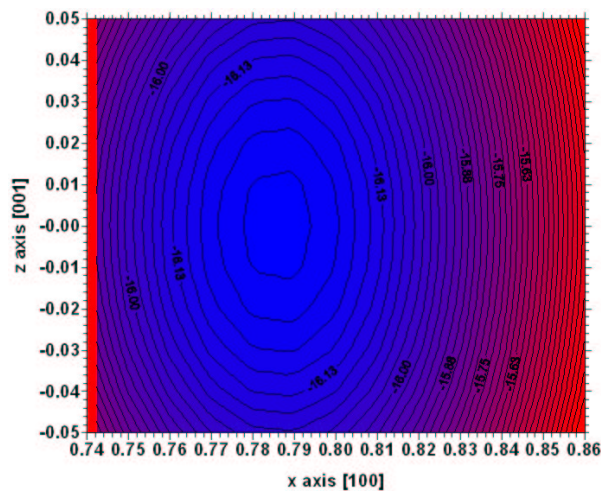
4.4.3.4 Nickel Migration via an Interstitial Mechanism

Nickel interstitial migration was taken to start at $(\frac{1}{2}, 0, 0)$ in Wyckoff coordinates. Migration hops are to adjacent interstitial sites. In this case two possible migration paths were identified and studied. The activation energy is taken as the difference between the defect

enthalpy for the nickel interstitial defect at the equilibrium position and the saddle point. The defect enthalpy calculated for an equilibrium nickel interstitial is -17.367eV (see table 4.9).

Nickel Interstitial Mechanism 1. This migration is to $(1, \frac{1}{2}, 0)$ which is in the $[110]$ direction. The saddle point was found to be at $(0.786, 0.124, 0.0)$ and the defect energy at this point predicted to be -16.629eV. The activation enthalpy for this migration is therefore 0.738eV $(-16.629\text{eV} - (-17.367\text{eV}))$. This is a mode 1 hop.

The hop is not direct and a meaningful contour plot parallel to the hop path could not be obtained. A plot perpendicular to the hop path at the saddle point was constructed and is shown on figure 4.22.



there is no interstitial site along the hop route and it must therefore be due to substantial lattice relaxation around the nickel interstitial defect.

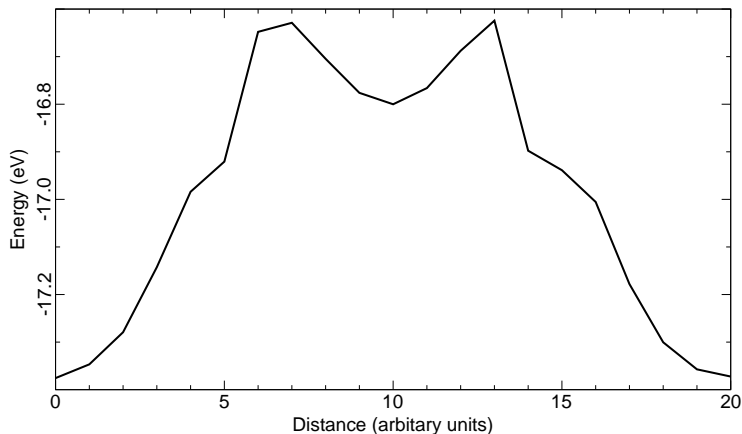


Figure 4.23: Activation energy plot for a hop via nickel interstitial mechanism 1.

Nickel Interstitial Mechanism 2. This migration is to $(\frac{1}{2}, 0, \frac{1}{2})$ which is in the [001] direction. The saddle point was found to be at $(\frac{1}{2}, 0, \frac{1}{4})$ and the defect energy at this point was determined to be -16.943eV. The activation enthalpy for this migration hop was therefore 0.424eV (-16.943eV - (-17.367eV)). This is a mode 1 mechanism.

This is a more regular hop with a well defined direct path as indicated by the contour plots in figure 4.24. No deviation from a straight line path is seen. The defect energy along the hop path varies smoothly to a maximum. As such the saddle point energy is clearly indicated.

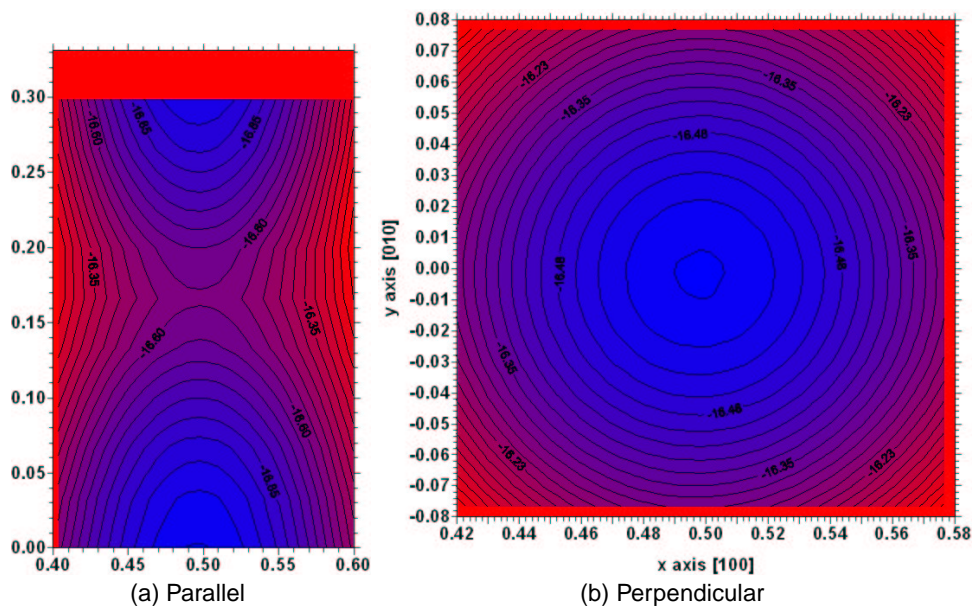


Figure 4.24: Energy contour plots parallel (a) and perpendicular (b) to a hop via nickel interstitial mechanism 2.

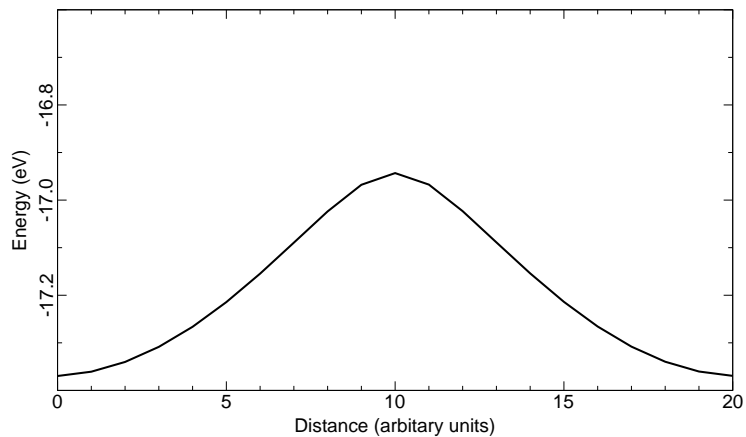


Figure 4.25: Activation energy plot for a hop via nickel interstitial mechanism 2.

4.4.3.5 Discussion of Migration Mechanisms

From the mechanisms investigated (see table 4.11), the lowest saddle point energy (0.024 eV) is consistent with fluorine interstitial ions migrating along the c-axis. The next lowest

saddle point energy also corresponds to fluorine interstitial migration, but now in the ab plane with only a marginally higher saddle point energy, (0.11eV).

Transport of fluorine via a vacancy mechanism is a much higher energy process. Migration pathways leading to long range transport were identified, the lowest energy being 0.67eV in the $[125\bar{24}125]$ direction. A lower saddle point energy exists in the [110] direction but this is not contiguous.

The most mobile nickel species are interstitial ions migrating in the c-axis, for which the energy is 0.42 eV. Transport of nickel in the ab plane has a significantly higher energy, 0.74 eV. Thus, transport of nickel is anisotropic and exhibits a much higher activation energy than fluorine. However, interstitial (and generally nickel vacancy) migration proceeds between low energy octahedral sites and tetrahedral saddle points. As such, there is an additional ligand-field term of approximately 0.9eV [66]. Thus, ligand-field energies will increase predicted cation migration energies significantly and may alter predicted migration pathways.

4.4.4 Extrinsic Defect Behaviour

Real engineering structures are not formed from pure materials. Pure metals in particular have very poor mechanical properties. As such, the necessary alloy additions will make their way into passive layers. Here the effect of impurities, or additions, on the defect properties of the NiF₂ passive layer are examined in detail. These are known collectively as extrinsic reactions.

4.4.4.1 Presentation of Extrinsic Results

Beginning with divalent cations, no compensation is required for their solution since they are isovalent with Ni²⁺. The normalised reaction sum, described by reaction 4.8, and its

individual components are given in table 4.12. Components of the monovalent cation solution reactions, described in equations 4.9-4.11, are given in table 4.13, assuming defects are isolated; and normalised data for monovalent solution mechanisms are presented in tables 4.14-4.22, assuming neutral defect cluster formation. For trivalent cation solution in NiF_2 , isolated components of the reactions 4.12 and 4.13, are given in table 4.23, assuming isolated defects; and normalised data for trivalent solution mechanisms are presented in tables 4.24-4.29, assuming neutral defect clusters.

As tables 4.13-4.29 show for each reaction there are a multitude of defect cluster configurations which must be simulated. However, the majority of these are unimportant and will be discarded as unfavourable. As such, the most favourable results are presented graphically as normalised solution energy (y-axis) vs. dopant cation radii (x-axis). Figure 4.26a shows isolated defect results and figure 4.26b shows clustered defect results. In these figures squares (■) denote dopant interstitial compensation, circles (●) denote interstitial compensation and inverted triangles (▼) denote vacancy compensation. The colour blue represents 1+ cation solution results and red represents 3+ cation solution results. The colour black and the asterisk (*) represents results for 2+ cation solution. The horizontal dashed line (at 2.26eV) indicates the value of the normalised anion Frenkel equilibrium energy. Two further solid horizontal lines (at 0.5 eV and 0.25 eV) correspond to solution limits of approximately 500ppm and 2,500ppm respectively (see section 4.3.2 for a detailed discussion of the significance of these limits).

Table 4.12: Isolated substitutional, fluoride lattice and solution energies for divalent cations in the host NiF₂ lattice.

Cation B_{Ni}^{\times}	Cation Radii (Å)	Lattice Energy (eV)	Substitutional Energy (eV)	Solution Energy (eV)
Ni ²⁺	0.69	-29.955	0.00	0.00
Mg ²⁺	0.72	-30.123	-0.22	-0.05
Co ²⁺	0.745	-29.469	0.49	0.01
Fe ²⁺	0.78	-29.136	0.84	0.02
Mn ²⁺	0.83	-28.341	1.70	0.09
Cd ²⁺	0.95	-27.348	2.90	0.30
Ca ²⁺	1.00	-27.094	3.36	0.50
Ba ²⁺	1.35	-23.941	8.13	2.11

Table 4.13: Isolated interstitial defect, substitutional defect and fluoride lattice energies (eV) for monovalent cations in NiF₂.

Monovalent Cation	Li ⁺	Na ⁺	Ag ⁺	K ⁺	Rb ⁺	Cs ⁺
Cation Radii (Å)	0.76	1.02	1.15	1.38	1.52	1.67
iso A_i^{\bullet}	-5.56	-2.94	-1.48	0.63	1.16	2.81
iso A'_{Ni}	15.80	17.12	17.99	19.38	20.37	21.99
Lattice En.	-11.13	-9.72	-9.22	-8.45	-8.03	-7.91

Table 4.14: $\{A'_{Ni} : A_i^{\bullet}\}^{\times}$ cluster energies (eV) for monovalent cation solution in NiF₂ via neutral dopant interstitial compensation (reaction 4.9).

Monovalent Cation	Li ⁺	Na ⁺	Ag ⁺	K ⁺	Rb ⁺	Cs ⁺
Cation Radii (Å)	0.76	1.02	1.15	1.38	1.52	1.67
Isolated	10.23	14.19	16.51	20.01	21.53	24.80
1st	8.45	12.63	14.74	17.86	19.85	22.97
2nd	8.45	12.63	14.74	17.86	19.85	22.97
3rd	9.52	13.49	15.80	17.86	19.85	23.69

Table 4.15: Solution energies (eV) for monovalent cations in NiF₂ via neutral dopant interstitial compensation (reaction 4.9).

Monovalent Cation	Li ⁺	Na ⁺	Ag ⁺	K ⁺	Rb ⁺	Cs ⁺
Cation Radii (Å)	0.76	1.02	1.15	1.38	1.52	1.67
Isolated	1.27	1.83	2.50	3.48	3.82	5.34
1st	0.38	1.06	1.62	2.40	2.97	4.42
2nd	0.38	1.06	1.62	2.40	2.97	4.42
3rd	0.91	1.49	2.14	2.40	2.97	4.78

Embolded results indicate the lowest solution energy geometry.

Table 4.16: Binding energies (eV) for neutral clusters, $\{A'_{Ni} : A_i^\bullet\}^\times$, in NiF₂: dopant interstitial compensation of 1+ cations (reaction 4.9).

Monovalent Cation	Li ⁺	Na ⁺	Ag ⁺	K ⁺	Rb ⁺	Cs ⁺
Cation Radii (Å)	0.76	1.02	1.15	1.38	1.52	1.67
1st	0.89	0.78	0.88	1.07	0.84	0.92
2nd	0.89	0.78	0.88	1.07	0.84	0.92
3rd	0.36	0.35	0.36	1.07	0.84	0.56

Embolded results indicate the highest binding energy geometry.

Table 4.17: $\{2A'_{Ni} : Ni_i^{\bullet\bullet}\}^\times$ cluster energies (eV) for monovalent cation solution in NiF₂ via neutral interstitial compensation (reaction 4.10).

Monovalent Cation	Li ⁺	Na ⁺	Ag ⁺	K ⁺	Rb ⁺	Cs ⁺
Cation Radii (Å)	0.76	1.02	1.15	1.38	1.52	1.67
Isolated	14.24	16.88	18.61	21.40	23.36	26.60
1-1	9.64	13.14	15.07	18.09	20.19	23.57
1-2a	10.14	13.52	15.36	18.23	20.23	23.44
1-2b	9.58	13.44	15.32	18.26	20.29	24.05
1-3a	9.53	14.28	16.07	18.77	20.60	23.83
1-3b	10.35	13.70	15.50	18.33	20.32	23.57
2-2a	8.46	14.31	16.17	19.02	20.92	23.79
2-2b	9.65	13.82	15.58	18.31	20.24	23.76

(continued on next page)

(continued from previous page)

Monovalent Cation	Li ⁺	Na ⁺	Ag ⁺	K ⁺	Rb ⁺	Cs ⁺
Cation Radii (Å)	0.76	1.02	1.15	1.38	1.52	1.67
2-2c	10.98	13.91	15.70	18.55	20.57	23.90
2-3a	9.58	14.54	16.26	18.84	20.66	23.53
2-3b	10.14	14.34	15.97	18.52	20.32	23.03
2-3c	11.30	14.19	15.90	18.63	20.58	23.74
2-3d	9.84	14.20	15.90	18.61	20.53	23.67
3-3a	12.07	14.65	16.25	18.82	20.70	23.79
3-3b	12.16	14.64	16.29	19.02	20.99	24.29
3-3c	12.01	14.59	16.26	18.97	20.92	24.15

Table 4.18: Solution energies (eV) for monovalent cations in NiF₂ via neutral interstitial compensation (reaction 4.10).

Monovalent Cation	Li ⁺	Na ⁺	Ag ⁺	K ⁺	Rb ⁺	Cs ⁺
Cation Radii (Å)	0.76	1.02	1.15	1.38	1.52	1.67
Isolated	2.18	2.12	2.37	2.78	3.16	4.16
1-1	0.65	0.87	1.19	1.68	2.10	3.15
1-2a	0.81	1.00	1.29	1.72	2.11	3.11
1-2b	0.63	0.97	1.27	1.73	2.13	3.31
1-3a	0.61	1.25	1.52	1.91	2.23	3.23
1-3b	0.89	1.06	1.33	1.76	2.14	3.15
2-2a	0.25	1.27	1.55	1.99	2.34	3.22
2-2b	0.65	1.10	1.36	1.75	2.11	3.21
2-2c	1.09	1.13	1.40	1.83	2.23	3.26
2-3a	0.63	1.34	1.58	1.93	2.25	3.13
2-3b	0.82	1.27	1.49	1.82	2.14	2.97
2-3c	1.20	1.22	1.47	1.86	2.23	3.20
2-3d	0.71	1.23	1.47	1.85	2.21	3.18
3-3a	1.46	1.38	1.58	1.92	2.27	3.22
3-3b	1.49	1.37	1.59	1.99	2.36	3.39
3-3c	1.44	1.36	1.58	1.97	2.34	3.34

Embolded results indicate the lowest solution energy geometry.

Table 4.19: Binding energies (eV) for neutral clusters, $\{2A'_{Ni} : Ni_i^{\bullet\bullet}\}^{\times}$, in NiF₂: interstitial compensation of 1+ cations (reaction 4.10).

Monovalent Cation	Li ⁺	Na ⁺	Ag ⁺	K ⁺	Rb ⁺	Cs ⁺
Cation Radii (Å)	0.76	1.02	1.15	1.38	1.52	1.67
1-1	1.53	1.25	1.18	1.10	1.06	1.01
1-2a	1.37	1.12	1.08	1.06	1.05	1.05
1-2b	1.55	1.15	1.10	1.05	1.02	0.85
1-3a	1.57	0.87	0.85	0.88	0.92	0.92
1-3b	1.30	1.06	1.04	1.02	1.01	1.01
2-2a	1.93	0.85	0.81	0.79	0.82	0.94
2-2b	1.53	1.02	1.01	1.03	1.04	0.95
2-2c	1.09	0.99	0.97	0.95	0.93	0.90
2-3a	1.55	0.78	0.78	0.85	0.90	1.02
2-3b	1.37	0.85	0.88	0.96	1.01	1.19
2-3c	0.98	0.90	0.90	0.92	0.93	0.95
2-3d	1.47	0.89	0.90	0.93	0.94	0.98
3-3a	0.73	0.74	0.79	0.86	0.89	0.94
3-3b	0.69	0.75	0.77	0.79	0.79	0.77
3-3c	0.74	0.76	0.79	0.81	0.82	0.82

Embolded results indicate the highest binding energy geometry.

Table 4.20: $\{A'_{Ni} : V_F^{\bullet}\}^{\times}$ cluster energies (eV) for monovalent cation solution in NiF₂ via neutral vacancy compensation (reaction 4.11).

Monovalent Cation	Li ⁺	Na ⁺	Ag ⁺	K ⁺	Rb ⁺	Cs ⁺
Cation Radii (Å)	0.76	1.02	1.15	1.38	1.52	1.67
Isolated	21.68	23.00	23.86	25.26	26.24	27.86
1st	20.31	21.80	22.64	23.86	24.65	25.77
2nd	20.36	21.84	22.71	24.01	24.87	26.18
3rd	21.10	22.45	23.34	24.76	25.76	27.40

Table 4.21: Solution energies (eV) for monovalent cations in NiF₂ via neutral vacancy compensation (reaction 4.11).

Monovalent Cation	Li ⁺	Na ⁺	Ag ⁺	K ⁺	Rb ⁺	Cs ⁺
Cation Radii (Å)	0.76	1.02	1.15	1.38	1.52	1.67
Isolated	1.43	1.38	1.57	1.88	2.16	2.91
1st	0.74	0.78	0.96	1.18	1.36	1.87
2nd	0.77	0.80	0.99	1.25	1.47	2.07
3rd	1.13	1.11	1.30	1.63	1.92	2.68

Embolded results indicate the lowest solution energy geometry.

Table 4.22: Binding energies (eV) for neutral clusters, $\{A'_{Ni} : V_F^\bullet\}^x$, in NiF₂: vacancy compensation of 1+ cations (reaction 4.11).

Monovalent Cation	Li ⁺	Na ⁺	Ag ⁺	K ⁺	Rb ⁺	Cs ⁺
Cation Radii (Å)	0.76	1.02	1.15	1.38	1.52	1.67
1st	0.69	0.60	0.61	0.70	0.79	1.04
2nd	0.66	0.58	0.58	0.62	0.69	0.84
3rd	0.29	0.27	0.26	0.25	0.24	0.23

Embolded results indicate the highest binding energy geometry.

Table 4.23: Isolated substitutional defect and fluoride lattice energies (eV) for trivalent cations in NiF₂.

Trivalent Cation	Al ³⁺	Cr ³⁺	Fe ³⁺	Mo ³⁺	Sc ³⁺	Y ³⁺	La ³⁺
Cation Radii (Å)	0.535	0.615	0.645	0.69	0.75	0.9	1.032
iso C_{Ni}^{\bullet}	-28.3	-27.39	-24.54	-23.02	-19.93	-15.79	-13.21
Lattice En.	-63.064	-62.104	-59.326	-57.835	-54.872	-51.113	-48.968

Table 4.24: $\{C_{Ni}^{\bullet} : F_i^{\prime}\}^{\times}$ cluster energies (eV) for trivalent cation solution in NiF₂ via neutral interstitial compensation (reaction 4.12).

Trivalent Cation	Al ³⁺	Cr ³⁺	Fe ³⁺	Mo ³⁺	Sc ³⁺	Y ³⁺	La ³⁺
Cation Radii (Å)	0.535	0.615	0.645	0.69	0.75	0.9	1.032
Isolated	-29.70	-28.76	-25.90	-24.38	-21.29	-17.15	-14.57
1st	-30.59	-29.63	-26.87	-25.44	-22.55	-18.59	-15.91
2nd	-30.19	-29.28	-26.71	-25.32	-22.34	-18.29	-15.56
3rd	-30.15	-29.23	-26.80	-25.44	-22.51	-18.54	-15.86
4th	-30.60	-29.64	-26.85	-25.46	-22.49	-18.45	-15.72
5th	-30.60	-29.29	-26.64	-25.44	-22.48	-18.54	-15.91

Table 4.25: Solution energies (eV) for trivalent cations in NiF₂ via neutral interstitial compensation (reaction 4.12).

Trivalent Cation	Al ³⁺	Cr ³⁺	Fe ³⁺	Mo ³⁺	Sc ³⁺	Y ³⁺	La ³⁺
Cation Radii (Å)	0.535	0.615	0.645	0.69	0.75	0.9	1.032
Isolated	1.71	1.70	1.74	1.75	1.82	2.00	2.22
1st	1.26	1.26	1.25	1.22	1.19	1.28	1.55
2nd	1.46	1.44	1.33	1.28	1.29	1.43	1.73
3rd	1.48	1.46	1.28	1.22	1.21	1.31	1.58
4th	1.26	1.26	1.26	1.21	1.22	1.36	1.65
5th	1.25	1.43	1.37	1.22	1.22	1.31	1.55

Embolded results indicate the lowest solution energy geometry.

Table 4.26: Binding energies (eV) for neutral clusters, $\{C_{Ni}^{\bullet} : F_i'\}^{\times}$, in NiF₂: interstitial compensation of 3+ cations (reaction 4.12).

Trivalent Cation	Al ³⁺	Cr ³⁺	Fe ³⁺	Mo ³⁺	Sc ³⁺	Y ³⁺	La ³⁺
Cation Radii (Å)	0.535	0.615	0.645	0.69	0.75	0.9	1.032
1st	0.44	0.44	0.49	0.53	0.63	0.72	0.67
2nd	0.24	0.26	0.40	0.47	0.53	0.57	0.49
3rd	0.23	0.24	0.45	0.53	0.61	0.70	0.64
4th	0.45	0.44	0.47	0.54	0.60	0.65	0.58
5th	0.45	0.27	0.37	0.53	0.60	0.69	0.67

Embolded results indicate the highest binding energy geometry.

Table 4.27: $\{2C_{Ni}^{\bullet} : V_{Ni}''\}^{\times}$ cluster energies (eV) for trivalent cation solution in NiF₂ via neutral vacancy compensation (reaction 4.13).

Trivalent Cation	Al ³⁺	Cr ³⁺	Fe ³⁺	Mo ³⁺	Sc ³⁺	Y ³⁺	La ³⁺
Cation Radii (Å)	0.535	0.615	0.645	0.69	0.75	0.9	1.032
Isolated	-30.71	-28.82	-23.11	-20.07	-13.89	-5.62	-0.46
1-1	-34.21	-32.34	-26.53	-23.45	-17.27	-9.06	-4.15
1-2a	-32.96	-31.12	-25.50	-22.48	-16.28	-7.76	-2.60
1-2b	-33.30	-31.45	-25.68	-22.59	-16.35	-8.07	-3.05
1-2c	-33.52	-31.66	-25.90	-22.85	-16.71	-8.63	-3.75
1-2d	-33.61	-31.74	-25.97	-22.93	-16.90	-9.49	-4.63
1-3a	-33.07	-31.20	-25.50	-22.47	-16.40	-8.51	-3.53
2-2a	-33.04	-31.17	-25.42	-22.36	-16.16	-7.78	-2.67
2-2b	-33.06	-31.18	-25.39	-22.33	-16.21	-8.50	-3.50
2-2c	-33.09	-31.22	-25.46	-22.41	-16.25	-8.06	-3.06
2-2d	-33.05	-31.18	-25.44	-22.41	-16.32	-8.59	-3.60
2-2e	-32.08	-30.27	-24.66	-21.66	-15.48	-6.95	-1.71
2-3a	-32.17	-30.31	-24.63	-21.63	-15.59	-7.63	-2.48
2-3b	-32.63	-30.75	-25.05	-22.02	-15.94	-7.99	-2.89
3-3a	-32.11	-30.23	-24.55	-21.53	-15.39	-7.29	-2.10
3-3b	-32.22	-30.34	-24.69	-21.71	-15.75	-8.04	-2.85

Table 4.28: Solution energies (eV) for trivalent cations in NiF₂ via neutral vacancy compensation (reaction 4.13).

Trivalent Cation	Al ³⁺	Cr ³⁺	Fe ³⁺	Mo ³⁺	Sc ³⁺	Y ³⁺	La ³⁺
Cation Radii (Å)	0.535	0.615	0.645	0.69	0.75	0.9	1.032
Isolated	1.85	1.84	1.89	1.91	2.00	2.25	2.54
1-1	0.69	0.67	0.75	0.78	0.87	1.10	1.31
1-2a	1.10	1.07	1.10	1.11	1.20	1.53	1.82
1-2b	0.99	0.96	1.04	1.07	1.18	1.43	1.68
1-2c	0.91	0.90	0.96	0.98	1.06	1.24	1.44
1-2d	0.88	0.87	0.94	0.96	0.99	0.96	1.15
1-3a	1.07	1.05	1.10	1.11	1.16	1.29	1.52
2-2a	1.08	1.06	1.12	1.15	1.24	1.53	1.80
2-2b	1.07	1.06	1.13	1.16	1.22	1.29	1.53
2-2c	1.06	1.04	1.11	1.13	1.21	1.43	1.67
2-2d	1.07	1.06	1.12	1.13	1.19	1.26	1.49
2-2e	1.40	1.36	1.38	1.38	1.47	1.80	2.12
2-3a	1.37	1.35	1.39	1.39	1.43	1.58	1.86
2-3b	1.21	1.20	1.25	1.26	1.31	1.46	1.73
3-3a	1.39	1.37	1.41	1.43	1.50	1.69	1.99
3-3b	1.35	1.33	1.37	1.37	1.38	1.44	1.74

Embolded results indicate the lowest solution energy geometry.

Table 4.29: Binding energies (eV) for neutral clusters, $\{2C_{Ni}^{\bullet} : V_{Ni}''\}^{\times}$, in NiF₂: vacancy compensation of 3+ cations (reaction 4.13).

Trivalent Cation	Al ³⁺	Cr ³⁺	Fe ³⁺	Mo ³⁺	Sc ³⁺	Y ³⁺	La ³⁺
Cation Radii (Å)	0.535	0.615	0.645	0.69	0.75	0.9	1.032
1-1	1.17	1.17	1.14	1.13	1.13	1.15	1.23
1-2a	0.75	0.77	0.80	0.80	0.80	0.71	0.72
1-2b	0.86	0.88	0.86	0.84	0.82	0.82	0.86
1-2c	0.94	0.94	0.93	0.93	0.94	1.00	1.10
1-2d	0.97	0.97	0.95	0.95	1.00	1.29	1.39
1-3a	0.79	0.79	0.80	0.80	0.84	0.96	1.02
2-2a	0.78	0.78	0.77	0.76	0.76	0.72	0.74

(continued on next page)

Embolded results indicate the highest binding energy geometry.

(continued from previous page)

Trivalent Cation	Al ³⁺	Cr ³⁺	Fe ³⁺	Mo ³⁺	Sc ³⁺	Y ³⁺	La ³⁺
Cation Radii (Å)	0.535	0.615	0.645	0.69	0.75	0.9	1.032
2-2b	0.78	0.78	0.76	0.75	0.77	0.96	1.01
2-2c	0.79	0.80	0.79	0.78	0.79	0.82	0.87
2-2d	0.78	0.78	0.78	0.78	0.81	0.99	1.05
2-2e	0.46	0.48	0.52	0.53	0.53	0.44	0.42
2-3a	0.49	0.49	0.51	0.52	0.57	0.67	0.68
2-3b	0.64	0.64	0.65	0.65	0.68	0.79	0.81
3-3a	0.47	0.47	0.48	0.49	0.50	0.56	0.55
3-3b	0.50	0.51	0.53	0.55	0.62	0.81	0.80

Embolded results indicate the highest binding energy geometry.

4.4.4.2 Isovalent Solution

With reference to equation 4.8 it is clear that divalent cation substitution requires no charge compensation. Consequently solution proceeds without impacting on the fluorine interstitial or vacancy concentration.

Solution energies for divalent cations, reported in figure 4.26a, show that ions close to the ionic radii of Ni (i.e. Mg²⁺, Co²⁺, Fe²⁺ and Mn²⁺) have very low solution energies and thus, high solution limits. This is evidenced by their solution energies being below the first horizontal black line set at 0.25eV. Larger ions, such as Cd²⁺ and Ca²⁺ have higher solution energies and will have lower solution limits. Here this is defined as being between the 1st and 2nd solid black horizontal lines. Solution energies of very large ions, like Ba²⁺, are so high that they are not expected to exhibit any appreciable solution limit, and they will only contribute to second phase formation.

Purely on this argument Mg, Co, Fe and Mn maybe suitable as major alloying additions, with Cd and Ca as minor or micro alloying additions to nickel. Ba can be discounted. The practicality of using these elements in a nickel alloy will be discussed later before making a final selection. Other candidate elements, not explicitly modelled, will also be

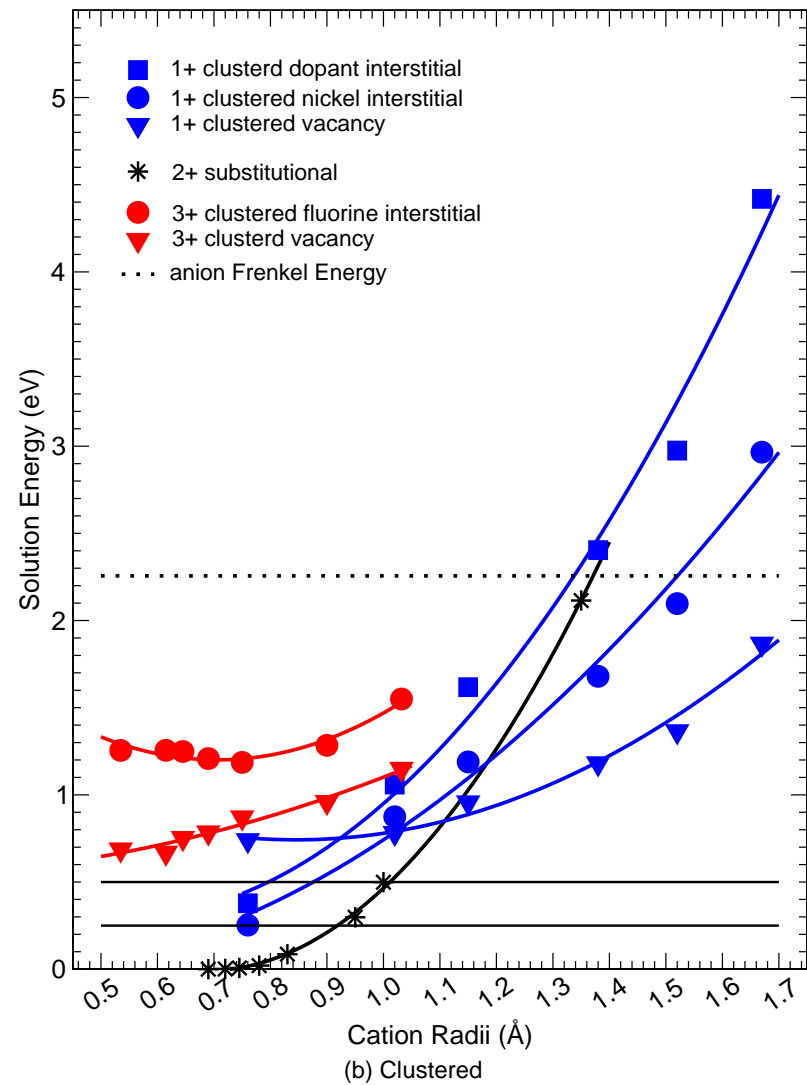
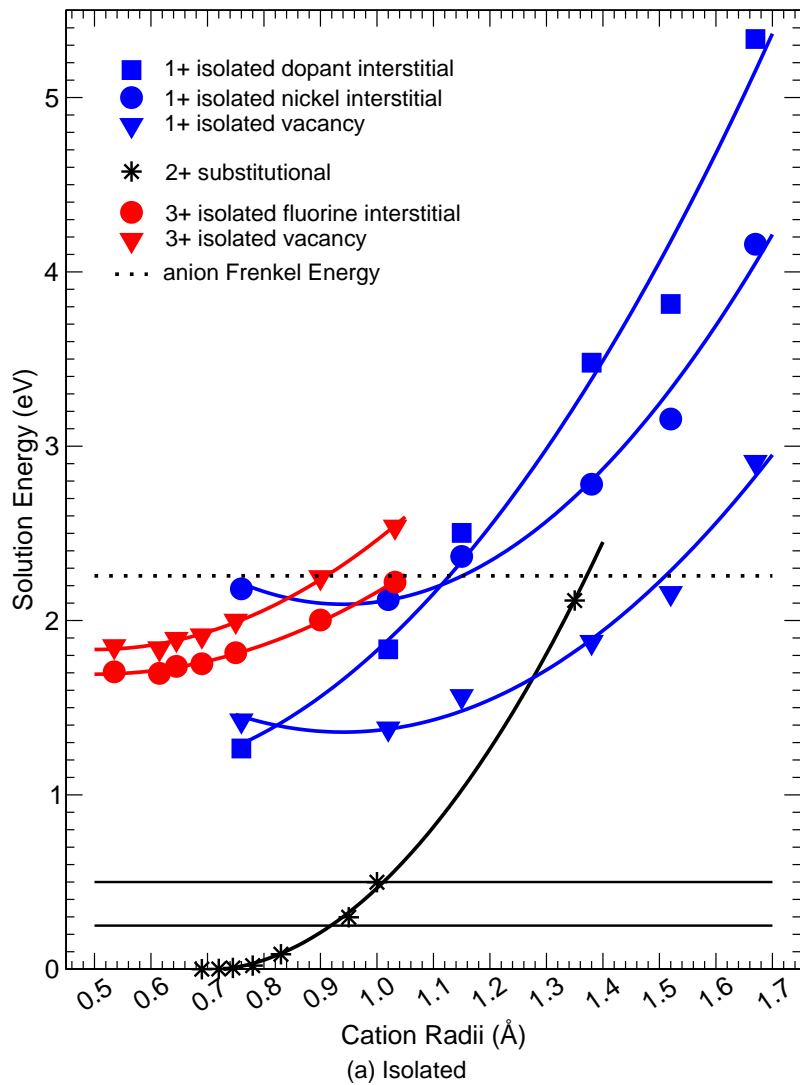


Figure 4.26: Normalised solution energetics of NiF_2 .

surveyed based on the identified trend of solution energy vs. cation radii.

4.4.4.3 Aliovalent Solution

As already stated, equations 4.9-4.13 show that solution of monovalent and trivalent impurities require charged compensating defects to maintain neutrality in the lattice. Figures 4.26a and 4.26b present normalised solution energies for the isolated and clustered case respectively.

4.4.4.4 Monovalent Impurities

Monovalent substitutional defects (A'_{Ni}) can be compensated by dopant interstitials, (A'_i), nickel interstitial ions (Ni''_i) or fluorine vacancies (V'_F) as shown in equations 4.9-4.11. Through the intrinsic defect equilibria (equations 4.1-4.3) it follows that the fluorine interstitial concentration will be reduced if compensation is by Ni''_i or V'_F but will be unchanged if compensation is by A'_{Ni} . This is important since it is desirable to limit or reduce the fluorine interstitial concentration.

Figure 4.26a shows that, if isolated defects are assumed, monovalent ions entering solution will be compensated by either dopant interstitials or fluorine vacancies depending on the ion radii. Dopant interstitial compensation is predicted below 0.83Å (i.e. for Li^+ only) and fluorine vacancy compensation is predicted above 0.83Å (i.e. for all other ions investigated explicitly here).

For vacancy and nickel interstitial compensation a minimum is observed in the monovalent solution energy curves at a radii slightly larger than the nickel cation radii. This is expected since substitutional ions that match the size of the substitutional site will introduce less strain (other energy terms do not depend on dopant size). The slight discrepancy arises since the effective size of the substitutional site, if occupied by a monovalent ion, is larger than if it is occupied by a host divalent cation. This is because the adjacent fluorine

ions will relax away from the substitutional defect since the effective charge is minus one. This minimum is not observed in the dopant interstitial curve, since this is dominated by the size of the interstitial ion which is larger than the interstitial site, even for Li^+ .

When clustering is introduced into the model (figure 4.26b) an overall reduction in solution energy, by up to 2.5 eV, is observed. This has the effect of increasing the ion size range at which dopant interstitial compensation is dominant over fluorine vacancy compensation. However, much more significantly the nickel interstitial compensation curve is so greatly effected by cluster formation that it now falls rapidly with decreasing ion radii, in contrast to the minimum it forms in the isolated case. Consequently, nickel interstitial compensation is now a lower energy process than fluorine vacancy compensation at ion radii below 1.2Å.

This behaviour, in the nickel interstitial mechanism, is accounted for by an observed change in defect cluster geometry which is only seen for Li solution. The 2-2a cluster geometry has a very anisotropic relaxation such that the two substitutionals associate at a Ni lattice site and the compensating Ni interstitial relaxes to fill the vacancy left behind by one of the substitutionals. Thus, a split substitutional (i.e. two interstitial ions adjacent to a lattice cation vacancy) is formed (see figure 4.27). This defect is the cation equivalent to the split fluorine interstitial defect observed in this material during earlier investigation of intrinsic properties (compare figure 4.27 and figure 4.3).

In the case of the competing dopant interstitial mechanism, closer examination of the final relaxed geometry reveals the formation of the same split substitutional defect. However, in this mechanism the relaxation is easier and larger ions also relax to form a split substitutional defect. This accounts for the very similar clustered lithium solution results for both nickel interstitial and dopant interstitial mechanisms. The stability of the split substitutional defect structure is further illustrated by the dopant interstitial data. In some cases the 2nd and 3rd third neighbour clusters relax to this completely different geometry.

In tables 4.15 and 4.16 clusters that relax to this split substitutional, which happen to be the lowest energy geometry, are embolded.

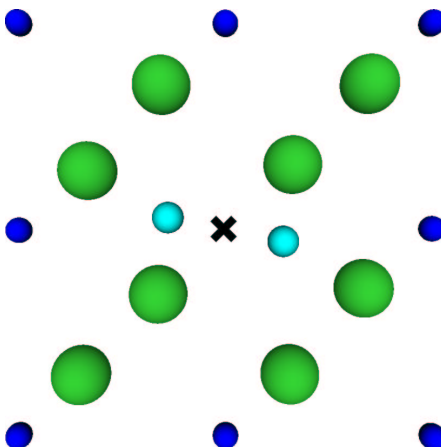


Figure 4.27: Representation of a split lithium substitutional defect in NiF_2 . Blue spheres are nickel ions, green spheres are fluorine ions and cyan spheres are lithium ions. The \times indicates the position of the vacant lattice site.

As in the monovalent case candidate alloying elements can now be selected. However, only Li can be selected as a significant alloying addition although Na may be used as a very minor addition. The other elements studied will have very low solution limits and so are likely to form a second phase.

Li may have additional benefits to reducing fluorine interstitial transport in the NiF_2 system. A scenario can be envisaged where a Li interstitial may form a stable associate with a fluorine interstitial (i.e. $\{\text{Li}_i^\bullet:\text{F}_i'\}$), essentially forming a ‘trap’ which will hinder the migration of fluorine interstitials through the lattice. The depth of this trap would be the binding energy of a $\{\text{Li}_i^\bullet:\text{F}_i'\}$ cluster. When briefly simulated in for a 1st neighbour configuration, this was found to be 0.77eV, which is considerable.

4.4.4.5 Trivalent Impurities

Trivalent solution defects (C_{Ni}^{\bullet}) can be compensated by fluorine interstitials (F_i') or nickel vacancies (V_{Ni}'') as shown in equations 4.12 and 4.13. The intrinsic equilibria (equations 4.1-4.3) suggests that an increase in F_i' or V_{Ni}'' concentration will tend to increase the fluorine interstitial concentration.

Figure 4.26a shows that isolated F_i' defects will compensate trivalent substitutional defects for the range of ion radii investigated. Again, a minimum in the solution energy curves in figure 4.26a is evident, however, the minimum is at an ion radius slightly smaller than that of the host cation. This is because the effective substitutional site is smaller. The trivalent substitutional defect has an effective charge of plus one, thus, the neighbouring fluorine ions relax toward it creating a smaller substitutional site.

If clustered defects are assumed (see figure 4.26b) an overall reduction in all solution energy by 0.5eV to 1.5eV is seen. A larger reduction occurs in the nickel vacancy compensation solution energies such that it becomes the dominant mechanism at all radii. This change in mechanism is again the result of anisotropic relaxation in some of the fluorine interstitial cluster geometries.

When forming 1st and 2nd neighbour fluorine interstitial clusters with a trivalent substitutional ion, the split fluorine defect results in 7 fold coordination of the substitutional ion. This is so unfavourable that the relaxation acts to return the cation back to a 6 fold coordination. In the relaxation process the split interstitial defect is relocated further away. The net effect is a cluster with a smaller the binding energy. Consequently, the spatially close configurations for the nickel vacancy mechanism mean higher binding energies, and thus allow this mechanism to dominate (compare values in table 4.26 with values in table 4.29). Again, different starting geometries relax to the same lower energy cluster and are highlighted by multiple emboldened results in tables 4.25 and 4.26.

Since 3+ cations will act to increase the fluorine interstitial concentration none of them are selected as candidate elements. Note, only Al, Cr, and Fe could show any appreciable solution limit. Other 3+ elements studied have solution energies so high that they would introduce second phases.

4.4.5 Additional Considerations

Fe^{3+} has already been identified as an undesirable impurity but it is likely to be even more detrimental than other 3+ ions. Consider that Fe^{2+} has a very low solution energy (see figure 4.26a), suggesting that it will have a significant solution limit. If a large number of Fe^{2+} defects are incorporated and then change valence to Fe^{3+} , two very detrimental effects can be expected:

- 1 The concentration of fluorine interstitials will be increased.
- 2 The number of Fe^{3+} defects will be much higher than the equilibrium solution limit, as such, they are likely to come out of solution and form a second phase or initially a grain boundary phase.

Thus, Fe in any form, should be carefully excluded from the alloy and steps taken to remove any impurity trace. This will of course have implications for alloy production and cost.

A survey of other ions, not explicitly modelled, suggests that Cu^+ , with an ionic radii of 0.77Å, will have a low solution energy and will reduce the fluorine interstitial concentration. In this case the $\text{Cu}^+/\text{Cu}^{2+}$ valence change is not a problem as Cu^{2+} is isovalent with Ni^{2+} and so will not introduce any compensating defects. Additionally, the ionic radii of Cu^{2+} is 0.73 Å which is close enough to Ni^{2+} that the risk of second phase formation is low. No other elements were identified as suitable candidates using the criteria developed here.

4.4.6 Final Selection

Having identified a potential alloy chemistry, tuned to form the best possible passive layer, it must be further refined with selection based on knowledge of materials and the suitability of the candidate elements as alloying additions. Thus, Na is discounted since it is too volatile to be a practical addition. Thus the final alloy chemistry is arrived at : Ni(Li,Cu,Mg,Co,Mn).

4.5 Summary

- Impurities with larger ionic radii have large solution energies and are likely to form second phases which are considered deleterious to the effectiveness of a passivation layer.
- Smaller divalent ions will not introduce defects into the NiF₂ lattice and so should have no impact on the properties of a passive layer. These elements may be used as alloying additions provided their ion solution energies are low.
- Smaller monovalent ions will reduce the concentration of fluorine interstitials in the lattice, and furthermore, will form defects that could hinder fluorine migration through the lattice. Again these elements could be included as alloying additions provided their ion solution energies are low.
- If trivalent impurities enter solution in NiF₂ they will increase the fluorine interstitial concentration. Thus these ions must be excluded from the passive layer.
- Of particular detriment to the passivation layer is iron which can enter easily as a 2+ (i.e. it exhibits a high solubility) ion but if it undergoes a valence change it will drive up the fluorine interstitial concentration. It may also form a second phase.

Guided by the above criteria and traditional alloying rules a novel Ni(Li,Cu,Mg,Co,Mn) alloy may have improved corrosion resistance to fluoride attack. Furthermore, trace 3+ ions or 2+/3+ redox couples should be carefully excluded from any nickel alloy that may rely on the formation of a NiF₂ passivation layer for protection.

4.6 Further Work

This work has been rigorous in both computational effort and the range of possible defect types considered, however, there are still aspects of this study which could be refined with further simulation. One such area would be a detailed study of the types of split defects that form in this material. Both intrinsic and extrinsic split defects have been seen. While these have been treated as conventional point defects they are really more like defect clusters. Exactly how this impacts on traditional intrinsic defect equilibria reactions has not been explored here but deserves some attention. This is important as such defects are likely to feature in other fluoride materials with the rutile structure. The simulation of saddle point energies is accepted to be approximate in determining migration behaviour and as such it would be interesting to study this question with molecular dynamics. For the moment such computational expense is beyond the resources available to my research group.

Another aspect concerns the crystallography of second phases that may develop. For example, with the alkali halides, phases such as KNiF₃ and NaNiF₃ perovskite are well known [67]. The effect of including these lattice energies in the defect equilibria should be considered.

More difficult would be to model grain boundary structures and the associated simulation of fluorine migration along them. Both pure NiF₂ and doped boundaries might be considered. This would address the issue of how dopants at grain boundaries might aid or

resist transport of fluorine.

The most obvious and exciting area of further work would be to conduct a comparative trial of a series of nickel alloys based on the chemistry proposed here. This should be benchmarked against Monel and conventional nickel alloys. Such a study would provide the ultimate validation of this methodology and the conclusions drawn.